LIMITING FACTORS OF THE TENSILE STRENGTH OF ARAMID FIBERS

BY

KORHAN SAHIN

DISSERTATION

Submitted in partial fulfillment of the requirements
for the degree of Doctor of Philosophy in Aerospace Engineering
in the Graduate College of the
University of Illinois at Urbana-Champaign, 2017

Urbana, Illinois

Doctoral Committee:

Professor Ioannis Chasiotis, Chair and Director of Research
Associate Professor Huck-Beng Chew
Professor Philippe H. Geubelle
Professor John Lambros
Professor Nancy R. Sottos

ABSTRACT

The correlation between the evolution of crystallite orientation in aramid fibers during loading and their mechanical and failure behavior were investigated. Three types of as-spun aramid fibers and a heat-treated type were employed with initial distributions of crystallite orientations between 16.7º and 9.7º with respect to the fiber axis. These directly correlated with the initial moduli that were between 66 GPa and 119 GPa, with no correlation between the initial crystallite orientation distribution and the tensile strength values that ranged between 3.5 and 4.0 GPa. Cyclic loading of individual, 10 mm long, as-spun filaments increased their initial moduli, all converging to 100 GPa for all fiber types when cycled to 90% of their respective tensile strength values. This modulus value (100 GPa) corresponds to a stable crystallite orientation distribution of 11.6º. On the other hand, the initial unloading modulus of all fiber types when loaded to 90% of their tensile strength converged to ~165 GPa which approaches the theoretical modulus of 220 GPa for monopolymer aramids. This limit value of the unloading modulus also signifies the tightest crystalline domain orientation distribution of 6.6º with respect to the fiber axis. However, this orientation distribution is not retained upon unloading. On the other hand, as-fabricated, post-spun heat-treated fibers had a much higher initial modulus of 120 GPa, and an initial unloading modulus of 170 GPa after mechanical cycling to 90% of their tensile strength value, corresponding to 5.8º domain orientation distribution. In all aramid types, mechanical cycling increased the initial modulus by as much as 54% while leaving the tensile strength of each fiber type unaffected in the narrow range of the aforementioned initial values. Thus, the limiting orientation distribution of ~6º emerges as the controlling factor in tensile failure of this class of fibers. Tension tests conducted at different strain rates showed that the permanent orientation of crystalline domains at high strains/stresses scales inversely with the applied strain rate. Notably, at strain rates of 0.2-0.3 s^{-1} both as-spun and heat-treated fibers were linearly elastic until failure.

A hypothesis that the fiber tensile strength is controlled by preexisting defects was tested by examining the scaling of the tensile strength with the fiber gauge length for fibers with lengths in the range of 200 μm to 10 mm. Prior works that were limited to

fiber gauge lengths longer than 2 mm, have been inconclusive due to large data scatter for short fibers. Controlled tests conducted in this dissertation research with dedicated test apparatuses for small scale experimentation, demonstrated a constant tensile strength for gauge lengths as short as 200 μm, thus, implying that failure does not obey weakest link statistics that are descriptive of critical flaw-induced failure initiation. Notably, in short gauge length fibers (200 μm) of all aramid types failure initiation occurred near the skin-core interface, followed by extrusion of the fiber core from the skin. Thus, the microstructural differentiation between the fiber core and the skin presents a likely limiting factor in tensile strength of aramid fibers.

Finally, the shear strength of the fiber core was measured for the first time with novel experiments that were designed and implemented with the aid of surface micromachined Microelectromechanical Systems (MEMS) devices. Edge notches were milled out in individual fibers using a focused ion beam to generate a zone of uniform shear stress along the fiber, when the latter was subjected to uniaxial tension. The optimum specimen design and specimen geometry were guided by a finite element analysis to shape the notch tip such that the stress singularity is eliminated and a uniform shear dominant plane is achieved. These unique but also challenging experiments were carried out on aramid fibers with the lowest orientation of 16.7º resulting in average shear strength of 85±7.6 MPa.

In conclusion, this dissertation research established new experimental tools and methods to investigate the origin of failure initiation in aramid fibers manufactured under different conditions. A limiting orientation distribution angle was established for all aramid grades, including those that were subjected to heat treatment, while the skin-core interface was identified as the weak interface where failure may take place.

ACKNOWLEDGMENTS

I had the chance to learn from many patient teachers in my life who did not complain about answering my sometimes-never-ending questions. On behalf of all, I would like to express my gratitude to my committee members Professors Nancy Sottos, Philippe Geubelle, Huck Beng Chew, John Lambros and Ioannis Chasiotis for not only their precious feedback that shaped my research over years, but also for the great classes they teach every year to hundreds of engineering candidates and engineers, including myself. I would like to express my special thanks to Professor Lambros for spending time to share his teaching wisdom with me, the unexperienced teaching assistant of one of the courses he taught. Last but not the least, I am grateful to my advisor Professor Chasiotis. He was the advisor who taught me, who supported my exploratory ideas and who discussed and debated over the findings to help shape this dissertation. Thanks are also due to our collaborators Professor Satish Kumar and Dr. Han Gi Chae from Georgia Institute of Technology, Professor Assimina Pelegri from Rutgers University, Dr. James Singletary from DuPont, and Dr. James Zheng and Suzanne Horner from the Program Executive Office - Soldier. I also want to acknowledge the support by the Program Executive Office - Soldier under contract number W91CRB-16-C-0011, with Dr. James Zheng as the program monitor.

I would like to thank Nick and Jan who were the Masters students that worked with me in the early years of my study for their sincere friendship, without which it wouldn’t be possible to work endless hours in the lab. I always appreciated the atmosphere created by the Nanomechanics and Materials Research Group members I had the chance to interact with over years; Pavan, Salman, Nikhil, David, Dimitrios, Ankit, Julia, Fan, Sean, Kuo Kang, and finally Debashish. Sometimes a piece of research equipment, sometimes a meal, sometimes just coffee or tea over which we were sharing ideas, whatever it was we shared a lot with Debashish.

I am grateful to a number scientists at the Frederick Seitz Materials Research Laboratory for teaching me advanced materials characterization techniques and helping me develop additional experimental tools to be installed into the equipment for my experimental needs; namely Dr. Vania Petrova for Scanning Electron Microscopy, Dr. James Mabon and Dr. Mike Marshall for Focused Ion Beam Microscopy, Dr. Wacek Swiech and Dr. Honghui Zhou for Transmission Electron Microscopy, the late Dr. Scott MacLaren and Dr. Kathleen Walsh for Atomic Force Microscopy, Dr. Mauro Sardela for X-Ray Diffraction.

Special thanks are due to Aerospace Engineering Department administration; namely Staci McDannel, Kendra Lindsey, Diane Jeffers, Laura Gerhold for their support in all administrative issues and Lee Booher, Greg Milner, Stephen Mathine for their support in manufacturing of the tools required throughout my studies as well as being the friendly next-door neighbors of our laboratory.

My final thanks are to two great figures that shaped my life. I clearly remember getting angry multiple times after failing to decipher the words in a book as an illiterate kid and it was always my dear Grandmother who calmed me down telling me that soon I will not only learn to read but also assured me that the end of this way will be the highest education someone can get. Although learning is a life-long process, considering a PhD degree is the highest educational degree a university can offer I think she was pointing to these days in my life. Next comes Mustafa Kemal Ataturk, the founder of the Turkish Republic, whose famous quote “Science is the only true guide in life.” was written on a panel that I passed by everyday of my primary school life. I have tried to follow this guide all through my life and am indebted to this life changing lesson packed in one sentence.

To my family who make this planet the place to live and fuel every single mitochondrion in my body.

TABLE OF CONTENTS

LIST OF FIGURES

LIST OF TABLES

CHAPTER 1

INTRODUCTION

Aramid or aromatic polyamide fibers are high performance fibers known for their high specific strength and tensile modulus [1-4]. Aromatic polyamides are also called rigid rod polymers, or lyotropic polymers, as they show liquid crystallinity in solution form [5]. The fibers owe their high strength and stiffness to high molecular orientation along the fiber axis, which results in at least partial loading of the covalently bonded polymer backbone. Due to their high specific strength, modulus, high temperature stability, and cut resistance, aramid fibers have been employed in several applications such as tire reinforcements, composite pipes, cable shields, bullet proof vests and helmets, flame retardant protective equipment, and cut resistive clothing. In this research individual Kevlar® filaments with commercial designations K119, K29, KM2 and K49 were used as high quality study materials to investigate the factors that control the ultimate tensile strength of this class of fibers.

1.1 Structure and Fabrication of High Performance Aramid Fibers

The backbone of Kevlar® is composed of poly(p-phenylene terephthalamide) (PPTA) which is synthesized from p-phenylene diamine and terephthaloyl chloride [2,6,7]. The polycondensation product PPTA is washed, dried, and crushed before spinning. For better fiber properties PPTA with polydispersity of 2-3 is used to achieve a narrow distribution of chain lengths [8]. Paraorientation of the aromatic rings of the PPTA macromolecule causes the PPTA chains to be in the *trans* conformation. Moreover, rotation of the PPTA chain around the phenyl-carbonyl and phenyl-nitrogen bonds is restricted due to the interactions between sequential phenyl and amine segments resulting in a rigid rod-like structure [3,9-12]. Paraorientation of the aromatic rings not only results in rigid rod-like chains but also enable efficient packing resulting in a highly crystalline structure [2]. A weight-averaged molecular weight of 40000 g/mol is used for fiber production, resulting in a chain length of ~230 nm for a projected monomer length of 1.29 nm [8,11,13].

PPTA is dissolved in ≥99.8% sulphuric acid (H_2SO_4) to form the spinning solution, also called PPTA/H_2SO_4 dope [8,14]. A high concentration of H_2SO_4 is required to prevent chain scission by hydrolysis in the presence of water [15]. At 80°C, as the concentration of the polymer increases, the dope viscosity increases too until a maximum of ~9.5 wt% polymer concentration; up to this point the solution is isotropic. After this point, the solution shows an anomalous behavior with a sharp decrease in viscosity due to the formation of liquid crystalline domains. In this anisotropic regime, the rod-like macromolecules assemble in a parallel order along the backbone axis of the molecules to form nematic liquid crystallites [2,8,16]. As the dope polymer concentration increases, the viscosity increases again until 20 wt% concentration, at which point solid precipitates form in the solution. Spinning of fibers is performed close to this solubility limit (≈19.6 wt%) at 80°C with as many nematic liquid crystallites as possible, as these result in easier alignment of the molecular structure along the longitudinal axis of the fiber [8,17].

PPTA macromolecules show strong intermolecular attraction. Their rigid rod-like structure suggests a limited number of conformations in the melt form resulting in a high melting point, before which the polymer is already degraded [8,18]. Therefore, conventional melt spinning cannot be utilized to fabricate PPTA fibers. Instead, the fibers are solution spun using a dry-jet wet spinning process [2,8], during which the solution is pushed through a spinneret into an air gap, finally entering a coagulation bath [19,20] as shown in Figure 1.1. The dope experiences shear flow through the spinneret, resulting in alignment of the nematic crystallites. Moreover, the presence of the air gap offers the opportunity of further alignment by stretching of the filaments through extensional flow. Drawing the filaments through the air gap results in significant increase in the Young's modulus of the PPTA yarn [17]. Although solidification may start as the filaments pass through the air gap [2], the exact state of the dope that enters the coagulation bath where fiber formation occurs is unknown [8]. During coagulation ~80wt% of the spinning solution is removed within the first 25 ms to result in crystallization of the nematic liquid crystals into long range highly oriented crystalline fibers. It has been shown that the orientation obtained through spinneret and the air gap is kept during coagulation as the high rate of coagulation prevents polymer relaxation, while the loss of a large amount of H_2SO_4 results in lateral shrinkage [17,21]. The remaining H_2SO_4 is removed by washing the fibers with water and by spraying with a neutralization agent, NaOH, after which the fibers were washed again by water to remove Na_2SO_4 [22]. Finally the fibers are dried at ~65°C to remove the absorbed water, which may be performed under a small amount of tension. Before winding into bobbins sizing may also be applied onto the fibers [8,15]. Although spun fibers do not require post-processing, a brief heat treatment above 350°C results in recrystallization and improves lateral order [23]. It has been reported that the highest modulus yarns, K49, are hot drawn after spinning [15].

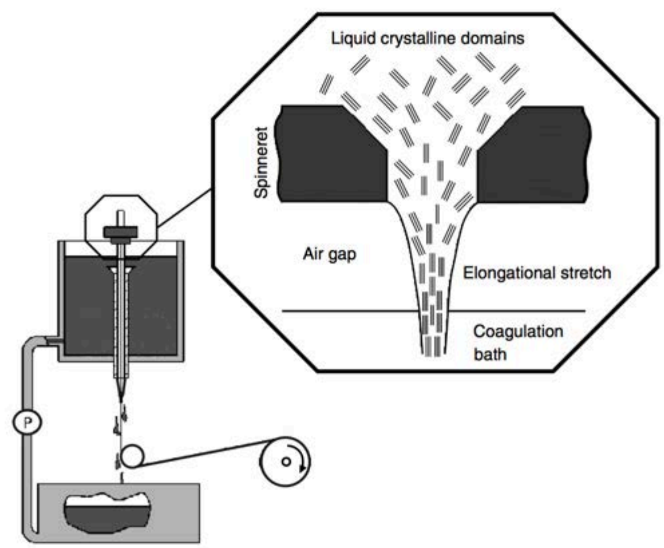

Figure 1.1 Evolution of liquid crystalline domain structure during the dry-jet wet spinning process [24]. Reprinted with permission from Elsevier.

1.2 Structural Characteristics of Aramid Fibers

1.2.1 Crystal Structure

PPTA fibers are highly paracrystalline, which means crystallinity is observed with slight disorder in the long range instead of a two-phase structure composed of amorphous and crystalline domains. This is due to the H bonds between the chains in addition to the planar phenylene and amide groups that promote order without any amorphous phase [8,10]. This argument was supported by the lack of amorphous halos in XRD patterns of experimental PPTA fibers [10,18], although other studies suggested the existence of a small amount of amorphous phase between crystallites [25]. Northolt et al. span their experimental fibers from in-house prepared PPTA and heat-treated those at 500°C to study the structure of the fibers using X-Ray Diffraction (XRD) [10,11]. The XRD data fit to a monoclinic, or pseudo-orthorhombic unit cell structure with the lattice dimensions of a = 7.87 Å, b = 5.18 Å and c = 12.9 Å with $\gamma \approx 90°$ as shown in Figure 1.2. Chains are connected in the plane by H bonds to form H bonded sheets. These H bonded sheets stagger in the out-of-plane direction by van der Waals interactions as well as π-bond overlapping of phenylene segments [24,26].

Although the packing modes can vary for fibers heat-treated at a lower temperature, the lattice dimensions were found to be the same [11]. While the c-axis is approximately oriented along the fiber axis, a synchrotron XRD study of PPTA filaments with ~28 μm diameter showed a ~10° misorientation of the crystalline structure with respect to the fiber axis [27]. Using a scanning microdiffraction method across the cross-section of microdissected K29 and K149 fibers, it was shown that the (200) crystal planes are aligned toward the center of the fiber supporting a radially oriented structure along the b-axis of the crystallites [28]. Equatorial reflections of the X-Ray diffraction patterns of PPTA showed a crystallite size of 50 Å, while broadening of the meridional reflections pointed to a paracrystalline model with 1.7% distortion parameter and 700 Å crystallite length [12]. For K29 fibers the paracrystalline distortion parameter was measured to be 5.9%. Annealing of the fibers at 100-400°C for 15 min resulted in 4.6-5.2% paracrystalline distortion. Annealing at 400°C resulted in an increase of crystallinity from

67.6% to 74.6% with an increase in the lateral crystallite size, suggesting melting of crystallites and recrystallization in the lateral direction with heating [29].

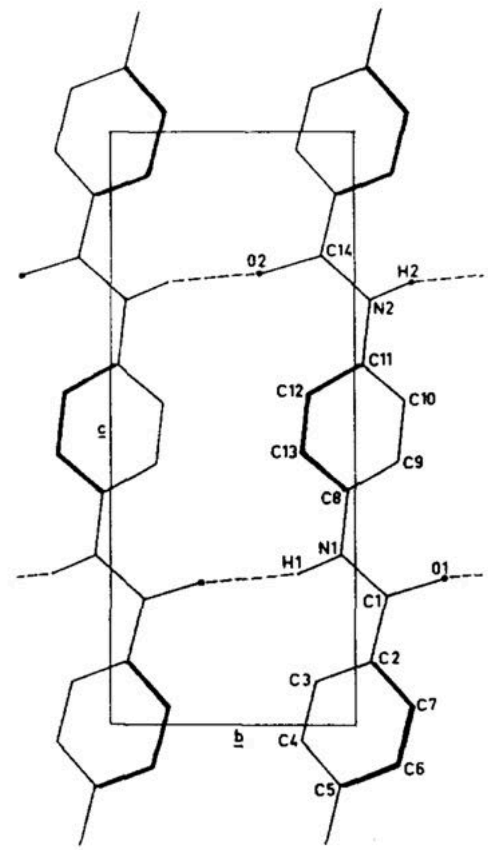

Figure 1.2 Monoclinic crystal structure of PPTA. The dashed lines between the monomers are the H bonds. H-bonded sheets stagger in the third direction due to van der Waals interactions and some π-bond overlapping of phenylene segments [11]. Reprinted with permission from Elsevier.

1.2.2 Mechanical Properties Derived from Crystal Structure

Estimating the mechanical properties of fibrous materials from their crystal structure has been the subject of numerous studies. For fibrous materials showing a two-phase sandwich structure of amorphous and crystalline domains, it is the amorphous regions that dictate the material properties; hence a Young's modulus an order of magnitude lower than the crystal lattice modulus is common. For aramid fibers, on the other hand, a one-phase paracrystalline model composed of crystallites interacting with secondary bonds is shown to describe the mechanical behavior satisfactorily [12].

The chain modulus, E_3, for a PPTA macromolecule was calculated as 220 GPa [12] following a calculation by Treloar [30] who took into account the effects of bond stretching and valence angle deformation. Assuming that the inter-chain interaction is predominantly due to H bonds, the transverse crystal modulus, E_1 and the shear modulus, *G,* values for PPTA were calculated as 16<E_1<29 GPa and 2.4<g<5.7 GPa [12]. Fielding-Russell, following Treloar's method, found $E_3 =$ 239 GPa, noting that this value can be as small as 200 GPa due to an overestimation associated with the calculation method [31]. Using the shift of the diffraction angle under loading for a bundle, assuming a uniform stress state over all fibers, the crystal lattice modulus for PPTA was calculated as 112 GPa. The extrapolation of sonic modulus measurements to a perfectly oriented fiber state gave a maximum fiber modulus of 160 GPa [12]. For these measurements, it should be noted that the inhomogeneous stress state inside the bundle may affect the measurement significantly, hence resulting in smaller measurements compared to the theoretical values.

Using the monoclinic structure of PPTA and cell dimensions measured by Northolt [10], XRD was utilized to measure the lattice strain at different stresses applied to PRD 49, an experimental PPTA fiber, calculating a 200 GPa crystal modulus along the chain direction [32]. The measured crystal modulus was close to that of an aliphatic polyamide fiber, nylon 6,6, while the observed Young's modulus values were much different, suggesting that the high Young's modulus of PPTA fibers cannot be explained simply by a stiff chain. A more recent study to model the PPTA fibers' mechanical behavior utilized Monte Carlo simulations. The fiber was constructed of a 3D array of units with primary modulus of 200 GPa and secondary shear modulus, due to H bonding, of 4.08 GPa. It was observed that the low number of secondary bonds along the length of the monomer limit the load transfer efficiency, and a higher molecular weight than 20000 g/mol is required to obtain higher modulus fibers [33].

Synchrotron X-Ray studies on single K49 fibers verified Northolt's monoclinic crystal structure: assuming the stress in the crystalline regions of the fiber to be equal to the applied stress on the fiber, the lattice modulus of the crystalline region along the polymer chains was measured to be 156 GPa for stresses below 1.1 GPa. The shift in the XRD peak due to the applied stress was perfectly reversible. At higher loads, the lattice modulus increased to 199 GPa. Considering that the orientation factor also increased with load, it was proposed that the increase in the tangent modulus is not only due to orientation improvement but also due to hardening, although the authors proposed that an orientation improvement due to stress should be ruled out [34]. WAXD patterns for PPTA fibers heat-treated to vary the Young's modulus showed a direct correlation with the paracrystalline distortion factor varying from 2.33% to 1.69% and the initial tangent modulus varying between 75-125 GPa. When the plot was extrapolated to 0% paracrystallinity, namely a single phase fiber with perfect crystallinity and perfect long range order, the modulus was deduced to be equal to 218 GPa which is close to the value measured for the PPTA crystal modulus [35].

Atomistic simulations and XRD studies of experimental fibers suggested the existence of polymorphs which were similar in structure due to the rigid rod-like nature of the chain [18,36]. Atomistic simulations for the allomorph closest to the crystal structure observed by Northolt provided E_1=21 GPa, E_2=13 GPa, E_3=270 GPa, G_1=4 GPa, G_2=19 GPa, G_3=5.6 GPa, ν_{12}=0.55, ν_{21}=0.86, ν_{13}= -0.94, ν_{31}= -0.07, ν_{23}=2.01, and ν_{32}=0.10, with x_3 being the chain direction, and the x_1 - x_3 plane lies with the H bonded sheets. E_1 was found to be larger than E_2 due to weaker van der Waals interactions along the x_2 direction. Using these crystal properties, a transversely isotropic fiber was modeled for which the chains were perfectly oriented along the fiber axis, while the transverse planes were randomly distributed in the cross-section. The elastic constants were calculated to be within the bounds: 270 GPa < E_3 < 330 GPa, 6.6 GPa <E_1=E_2 <22 GPa, 5.2 GPa <G_1=G_2< 14 GPa, 0.6 <ν_{12} = ν_{21} < 0.66, and 0.46<ν_{13} =ν_{23} <0.54 [37]. A more recent study using the same crystal elastic properties predicted 273 GPa <E_3< 335 GPa, 16.7 GPa <E_1=E_2 < 20.3 GPa, 6.7 GPa <G_1=G_2 <13.7 GPa, 0.62<ν_{12}=ν_{21}<0.66, and 0.4 <ν_1=ν_{23}<0.53. Averaging over the randomly oriented transverse properties gave the Hill-

Wallpole averages of E_3=309 GPa, E_1=E_2=19.7 GPa, G_1=G_2=12 GPa, ν_{12}=ν_{21}=0.62, and ν_{13}=ν_{23}=0.51 [38]. Although informative, these calculations do not take into account that crystallites cannot be perfectly oriented along the fiber, which results in overestimations. The transverse crystal properties have also been measured via using XRD. For instance, the Poisson ratio of K29 and K49 fibers was measured as $\nu_{31} = \nu_{32} = 0.31$ [39].

1.2.3 Supramolecular Structure and Skin-Core Differentiation

The supramolecular structure of PPTA fibers is fibrillar at the fiber core which is comprised of crystallites, while the chains are hypothesized to be more oriented in the skin region with randomly distributed chain ends lacking crystalline order [15,40]. Different conclusions have been reported for the core region: Morgan et al. proposed that the core is comprised of circular crystallites ~60 nm in width and ~250 nm long [15]. Using scanning tunneling microscopy (STM), Sawyer et al. observed a hierarchical fibrillar structure comprised of basic building blocks, microfibrils, in the form of 3-30 nm wide and 2-3 nm thick tapes [41]. In this hierarchical model, microfibrils comprise the fibrils (500 nm diameter) which, in turn, are the building blocks of macrofibrils (5 µm in diameter) that form the individual Kevlar® fibers. Panar et al. proposed a fibrillar structure of ordered lamella with defect zones at the chain level, with the fibrillar structure superimposed on a pleated sheet structure with a period of ~500 nm [42].

Dobb et al. [43] further showed by electron diffraction and dark field imaging of K49 that the sheet structure may form an angled pleated structure with sheets of ~500 nm period that are radially oriented. Polarized light diffraction experiments on single K49 filaments showed a decreasing scattered light intensity with increasing applied stress due to opening and straightening of the pleated structure [44]. Further examination of the measurements showed that the integrated light diffraction intensity was constant after 1.7 GPa applied stress. Considering mechanical conditioning experiments with K49 fibers which showed increasing modulus until ~2.2 GPa applied stress but remaining constant thereafter, that straightening of the pleated structure was proposed as the reason for increasing fiber modulus [44]. Further experiments on K29 and K149 fibers showed that the diffraction intensity profile becomes flatter with lower intensity as the fiber modulus increases. Cyclic loading experiments under polarized light suggested that the pleats can be restored by unloading and the opening and straightening of the pleats is an elastic process [44].

During coagulation, the periphery of the fibers may solidify rapidly forming a skin region [18]. Selected area diffraction profiles of microtomed sections of experimental PPTA fibers showed a gradual increase in crystalline orientation from the surface to the center of the fibers, while for the highly oriented, high modulus fibers, the difference was less pronounced [40]. Scanning microdiffraction applied to microdissected K29 and K149 samples showed a highly oriented periphery, while the change in orientation was gradual from the center to the surface, and the skin thickness was similar for K29 and K149 fibers [28].

1.2.4 Impurities and Defects in Fiber Structure

Defects in aramid fibers are divided into defects at the molecular scale and defects or structural irregularities at the fibrillar scale. Possible defect types are classified as isolated chain ends, side groups, voids, interstitials, and defect bands [9]. Among them, the isolated chain ends, the side groups, and the interstitials lie at the molecular level, while the voids and defect bands as well as clustered chain ends form weak defect planes at the fibril level. According to Morgan's model, failure starts at the highly ordered skin which is under higher stress due to its higher Young's modulus, and the cracks that form travel around the chains in the skin into the core at weak planes that facilitate propagation and catastrophic failure [15]. Existence of voids can be examined by measuring the density of fibers. The crystallographic density of PPTA is 1.48 g/cm^3 while the experimental fibers reported by Northolt et al. [10] showed a density of 1.44 g/cm^3 suggesting nonzero porosity in the fiber structure. Finally, using a floatation method, the density of K49 fibers was measured as 1.453 g/cm^3 [34].

1.3 Mechanical Behavior of Aramid Fibers

1.3.1 Elastic Behavior

Early work on modeling of the mechanical behavior of paracrystalline partially-oriented polymer fibers utilized aggregate theory of the transversely isotropic elastic domains that form a fiber. The domains were misaligned along the axis of the fiber with a distribution of orientation angles. Assuming conservation of domain volume during deformation and affine deformation, the Young's modulus of a fiber was calculated for an orientation-weighted aggregate of crystalline domains [45].

Northolt studied the evolution of orientation distribution of PPTA bundles under load by XRD and obtained bundle sonic modulus measurements using a pulse propagation technique; the sonic modulus of the bundle increased with applied strain while the orientation parameter was linear with the dynamic compliance [46]. Using aggregate theory for end-to-end connected crystallites along the fiber, which are described by an orientation distribution parameter, $\langle \sin^2\theta \rangle$, relative to the fiber axis, the fiber compliance, S_{33}, can be calculated as:

$$S_{33} = \frac{1}{E_3} + A \langle \sin^2 \theta \rangle \tag{1.1}$$

where A is a combined material property for the crystal defined as,

$$A = \frac{1}{G} - \frac{2(1 + \nu_{13})}{E_3} \tag{1.2}$$

where E_3 is the crystallite modulus along the chain axis, G is the shear modulus for a plane containing the axis of symmetry, and ν_{13} is the Poisson's ratio for a stress applied along the axis.

The Full Width at Half Maximum (FWHM) value for a Lorentzian fit to the azimuthal XRD profile for the (200) peak gives an accurate approximation of the orientation distribution parameter, $\langle \sin^2\theta \rangle$ as [46]:

$$\langle \sin^2 \theta \rangle = 2.1141 \ \sin^2\left(\frac{FWHM}{2}\right) \tag{1.3}$$

Measured dynamic compliance values vs. orientation parameter for bundles under loading showed the same linear relationship, as demonstrated in Figure 1.3 [46]. It was observed that E_3=240±10 GPa and A=0.26±0.01 m^2/ GN fit the data accurately for all PPTA fibers. Considering the anisotropy of the fibers, the value *1/A* will be a good approximation for the shear modulus, *G*, which would then be 3.8 GPa. One of the important results of this study is that for bundles undergoing loading for the second time, the dynamic modulus vs. orientation distribution parameter data lie on the same line fit as the first loading.

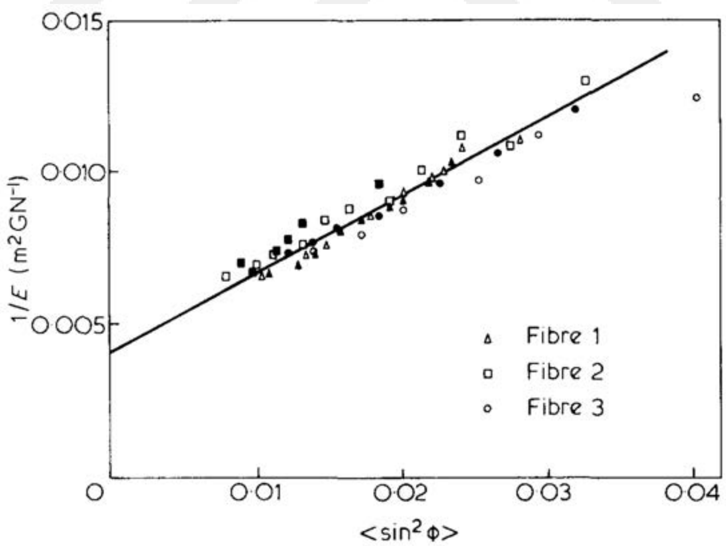

Figure 1.3 Dynamic compliance vs. orientation distribution parameter for bundles of PPTA with different Young's modulus. The filled marks demonstrate the behavior during the second loading [46]. Reprinted with permission from Elsevier.

Although aggregate models could explain the elastic fiber behavior, the deformation of neighboring crystalline domains does not satisfy continuity. Northolt et al.

proposed an improved aggregate model in which the fiber is comprised of parallel fibrils loaded uniformly along the length of the fiber that are composed of series-connected oblong transversely isotropic domains [47]. In this model, the elastic extension of the fiber was assumed to be the projection of the elastic extension of the chains in the crystalline domains, in addition to the shear deformation of the domains projected onto the fiber axis. The latter has a higher contribution due to the low crystalline shear modulus set by weak secondary interchain bonding. With this deformation definition, continuity between the domains was satisfied. As the fiber is loaded, the domains start rotating towards the fiber axis such that the orientation distribution becomes narrower and the fiber stiffens. Assuming strongly transversely isotropic domains, such that $E_3 >> G$ and $E_3 >> E_1$, the compliance of the fiber can be modeled as:

$$S_{33} = \frac{1}{E_3} + \frac{\langle \sin^2 \theta \rangle}{2G} \tag{1.4}$$

which is indeed very close to Equation (1.1).

Taking into account the deformation of all domains with varying misorientation angles in a fiber, the strain in the fiber, ε_f, under an applied stress, σ_f, can be calculated as:

$$\varepsilon_f = \frac{\sigma_f}{E_3} + \frac{\langle \sin^2 \theta \rangle}{2}\left(1 - e^{-\frac{\sigma_f}{G}}\right) \tag{1.5}$$

PPTA yarns with different Young's moduli were cyclically loaded to ~1.8 GPa. The reloading curves did not show any hysteresis suggesting that reloading is an elastic process. These elastic reloading curves could be modeled fairly well using Equation (1.5) using the measured orientation distribution factor at the beginning of reloading and E_3=240 GPa and G=2 GPa [47].

Further efforts to understand the elastic fiber behavior used finite deformation theory for a long chain of equal length segments forming domains with the surrounding chains and having an orientation distribution along the length. The elastic fiber behavior model could be further improved as [48]:

$$\varepsilon_f = \frac{1}{E_3} + \frac{\langle \sin^2\theta \rangle}{2G}\left(\frac{1}{1+\frac{\sigma_f}{2G}}\right) \quad (1.6)$$

Considering the long relaxation times of PPTA, the unloading curve was expected to represent a nonlinear but elastic process. It was shown that the unloading curve for a Twaron 1000 fiber can be predicted using Equation (1.6) [49].

Allen et al. [50] modeled the deformation of a fiber as the coupling of shear deformation to fiber extension due to the pleated structure resulting in periodic variation of orientation along the fiber axis. It was proposed that if the positive and negative values of misorientation angles for crystallites are equally probable, the tensile load could not be coupled to the shear deformation in the aggregate, hence fibrillar and microvoid nature of the structure should also be considered. The fiber modulus of highly-oriented fibers was found to follow:

$$\frac{1}{E} = \frac{1}{E_a} + \frac{(\tan^2\theta)}{G}\left(e^{-2\frac{\sigma}{G}}\right) \quad (1.7)$$

where $<tan^2\theta>$ is a measure of misorientation in the unloaded fiber and E_a is the highest fiber modulus measured using a stress perturbation experiment. This value is preferred over the crystal modulus as it describes the local order of the fiber close to failure. Equation (1.7) was shown to predict the elastic modulus of K49 using a misorientation angle for pleated structure as 4.5°, in the range of 4-5° [43]. The elastic constants were G=2 GPa, measured by torsion tests on single K49 fibers [51] and E_a=175 GPa, obtained from stress perturbation experiments.

1.3.2 Fiber Yielding

A typical curve for loading-unloading of PPTA fibers is demonstrated in Figure 1.4 for strain rates smaller than 0.05/min. The fiber stiffness decreases at ~0.4% strain when hysteresis also begins. When the strain exceeds the maximum strain applied in the previous loading step, the monotonic loading curve is then followed [46].

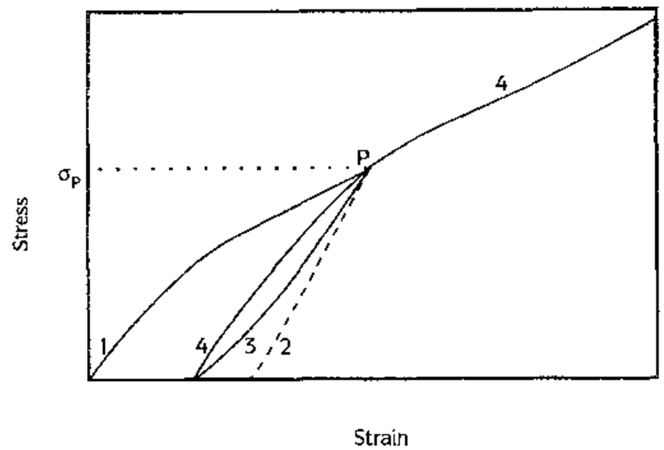

Figure 1.4 Loading-unloading curve for a PPTA fiber demonstrating hysteresis during reloading, but follows the monotonic stress-strain curve when the previous maximum applied stress is exceeded [52]. Reprinted with permission from Elsevier.

The orientation distribution parameter, $<sin^2\theta>$, for PPTA bundles decreased exponentially with increasing stress, suggesting a narrowed orientation distribution. More important was the observation that the orientation distribution of unloaded bundles was narrower than the pristine bundles, while reloading after complete unloading resulted in further orientation of the crystallites: during the first loading stage some crystallites rotated permanently towards the fiber axis, which was considered a yielding mechanism for PPTA fibers [46]. Tests with bundles unloaded from a maximum tensile stress value, followed by five minutes of relaxation, showed that the remnant strain upon unloading from the same stress level decreases for fibers with higher Young's modulus. As the fraction of misoriented crystallites is smaller for high Young's modulus fibers, this result further supports the idea of yielding originating in the permanent rotation of crystallites towards the fiber axis [46].

PPTA fibers with different orientation distributions had similar stress-strain behavior as in Figure 1.4. Although the nonlinearity was less pronounced for higher orientation fibers, the onset of nonlinear behavior was at similar strain levels which suggested that a shear strain criterion similar to Schmid's law for metals could be used to predict the onset of nonlinearity by calculating the resolved shear stress in misoriented crystallites. Fiber unloading in Figure 1.4 is not linear, while the reloading curve, 4, shows hysteresis up to the previously applied maximum stress, followed by the monotonic loading curve. Since the resolved shear stress is higher in crystalline domains with higher misorientation angle, it was proposed that as the tensile load increases the critical shear stress is reached for the highly misoriented domains which permanently rotate toward the fiber axis. When the fiber is unloaded and reloaded the response would be stiffer due to these permanently rotated domains. If the stress exceeds the previous maximum stress, domain rotation starts for the domains that have not rotated in the previous loading cycle, hence the stress-strain curve follows the monotonic curve [52]. The unloading curve was parabolic due to relaxation and nonlinear elasticity [52].

The yield in tensile stress-strain curves was explained by permanent local shear deformation of domains for which the resolved shear stress exceeds a critical value [53,54]. It was observed that the sonic modulus value at zero stress was close to the initial tangent modulus, suggesting viscoelasticity does not play a big role in the initial elastic deformation. However, the slope change with yielding requires further explanation. To this effect, a linear strain hardening law was utilized to model yielding and hardening in stress-strain curves [54].

In commercial Kevlar® fibers, monotonic tensile tests on K29 and K49 single fibers showed approximately constant tangent modulus until ~0.5% strain, after which point tangent modulus values increased while both fibers slightly softened before failure. Cyclic testing of K49 fibers showed no irreversible deformation below 0.5% strain. The reloading tangent modulus was higher up to the maximum stress applied in the previous cycle. After that point, the stress-strain behavior followed the monotonic loading curve. When K49 fibers were cycled to the same maximum stress applied in the previous cycle, no increase was detected in the irreversible deformation. The initial unloading modulus of K49 was much higher than the tangent loading modulus at the same strain due to time dependent effects [50].

The initial tangent modulus of mechanically conditioned K49 fibers was constant until ~2% strain. It was hypothesized that the increase in the modulus with mechanical conditioning was due to opening and straightening of the pleated structure. It was argued that an increase in the modulus could not be observed in a monotonic loading test because relaxation processes competed with opening of the pleats. A stress perturbation test following 30 s relaxation was performed on K49 to obtain modulus values that are less effected by time dependent processes. The modulus values measured this way were comparable to the unloading modulus further supporting the argument that the initial unloading modulus is an elastic property which is a measure of crystallite orientation distribution at that stress [50].

1.3.3 Compressive Properties

XRD studies of K49 fibers under compression also showed an orientation angle distribution change. Importantly, there was a linear relation between the measured birefringence and the FWHM under load suggesting that birefringence in Kevlar® fibers is mainly related to orientation effects due to changes in the alignment of crystallites, and in lesser degree to conformational changes of polymer chains [55]. Single K49 fibers bonded to the compressive strain side of polycarbonate beams under 3-point bending showed a compressive yield strength of 0.7 GPa. Further tests were performed by matrix shrinkage of solvent cast nylon for K49 fibers, which showed kink bands turning into slip bands at a compressive strain >3%. Fibers compressed to 3% via matrix shrinkage were then tested in tension approximately showing the same behavior as a pristine fiber after 2% tensile strain. The Young's moduli of compressed fibers were the same as pristine fibers with only ~10% loss in tensile strength. Tensile tests were also performed on fibers that passed through compressive fatigue cycles on a 4-point bend setup, 100 cycles to 1.2% compressive strain. This resulted in a 10% loss in strength, further proving that axial compression only results in a small loss of tensile strength. Tensile strength value remaining nearly constant whether the fiber kinked or not suggests that during kinking no chain scission is occurring, but that kinking is a process of bond rotation and bending resulting in microbuckling of the fibrils [56]. Kinked fibers tested in tension broke at the kink with only 25% reduction in tensile strength [57].

1.3.4 Transverse Mechanical Properties

The transverse mechanical properties of K29, and K49 filaments have been measured by compression of multiple parallel fibers between flat platens, which provided a transverse modulus of E_1=E_2=0.77 GPa for K29 and E_1=E_2=0.76 GPa for K49 [58]. A more recent measurement from a K29 single filament compressed by the same method was E_1=E_2=2.45±0.4 GPa [59], while for a single transversely compressed KM2 fiber this value was E_1=E_2=1.34±0.35 GPa. These values were an order of magnitude smaller than predicted by atomistic simulations, Section 1.2.2, possibly implying that the transverse properties are limited by voids in the fiber structure [60].

1.3.5 Shear Properties

The shear modulus and strength are important in the weaving process of aramid-based fabrics, which results in twisting of single filaments. Torsion tests with single 20 mm long K49 filaments yielded a shear modulus value of 1.8 GPa [56]. Further studies have shown that the shear modulus increases with applied tension [51]. Using Equation (1.7), the shear modulus of K29 was estimated as 1.8 GPa [50]. Permanent shear deformation occurred when K49 fibers were subjected to torsional shear strains exceeding 10% [56]. The irrecoverable shear strain, a remnant strain after the fibers were untwisted, increased approximately linearly with applied torsional after 10% shear strain and the fibers split axially following a helical path. The shear strength at the point of fiber splitting under torsion was estimated to be 180 MPa [56]. Considering the highest shear stress would be observed at the surface of a circular fiber, splitting should start at the surface and travel into the fiber with secondary bond failure and sliding of crystallites, which would result in cracks inside the fiber. Fibers that were pre-conditioned via twisting to <10% shear strain, maintained the tensile strength of pristine fibers. On the other hand, the tensile strength of fibers that were twisted to shear strains larger than

10%, decreased almost linearly with shear strain [56]. Finally, experimental PPTA fibers with varying tensile strengths showed shear strength values ~25-110 MPa [61].

1.4 Failure of High Performance Aramid Fibers

Earlier work on monotonic failure, creep rupture and fatigue of K29 and K49 fibers provided ample evidence of axial splitting. Notably, the length of axial splitting in fatigue tested fibers was up to seven times that measured in monotonic loading, providing some indirect evidence for interfibrillar secondary bond failure. It is further noted that the fatigue strength was only slightly smaller than the tensile strength [62-64]. On the other hand, the creep lifetime of single K49 filaments followed a 2-parameter Weibull distribution suggesting a weakest link failure model [65]. The activation energy measured from creep rupture lifetime tests on K49 fibers was estimated to be 335 kJ/mol; this value which is close to the energy required to break the C-N bond at the backbone, implies that chain scission could also contribute to creep failure [66].

Few studies concentrated on correlations between tensile strength and fiber microstructure and orientation. In a study by DuPont [67], fibers produced by various spinning and heat-treatment conditions with higher orientation also demonstrated higher strength. This relationship between the asymptotic modulus and strength was explained by using a maximum shear stress criterion for misoriented crystallites with a shear strength value of 170 MPa. The results suggested that failure is due to a critical resolved shear stress that is accentuated by anisotropy and crystallite misorientation [67]. The correlation between crystalline orientation and strength was demonstrated with experimental PPTA fibers that did not have significant skin-core difference. Further studies on Raman microscopy of experimental PPTA fibers showed that the Raman band shift should be due to chain stretching but not crystallite rotation. Considering the Raman signal is obtained 1-2 µm depth from the surface, the authors argued that the Raman band shift originated mostly in the skin regions where the chain orientation is higher than the core [40].

In a different interpretation of macroscopic properties, PPTA fibers fail at discontinuities resulting in amplification of shear stress that exceeds the shear strength of the secondary bonds [61]. This understanding was based on a partial correlation between the shear strength of experimental PPTA fibers with their tensile strength. Considering that fibers are comprised of end-to-end connected crystallites with an orientation distribution along the fiber axis, the less aligned the crystallites are the more voids would be present [46]. It was further speculated that voids would further hinder the rotation of crystallites, thus, amplifying the local stress in less oriented fibers [46]. A different study suggested that for large orientation differences between neighboring crystallites, rotation could only occur either due to voids or due to oriented or misoriented amorphous material between the crystallites [68]. The relative crystallite motion would result in further void formation or material flow in the intercrystalline region.

Raman studies with single K49 filaments and experimental PPTA fibers under stress reported a shift of the band (1610 cm^{-1}) corresponding to phenylene group stretching to lower wavenumbers, thus pointing to molecular deformation. The simultaneous broadening of the band suggested a non-uniform stress state [69-74]. Although band broadening may be due to a spectrum of misorientation angles, it may also stem from defects in the structure, which result in redistribution of load. Known defects are isolated chain ends, side groups and interstitials at the molecular level while voids and clustered chain ends may form weak planes at the fibrillar scale [9]. Small-angle X-Ray scattering (SAXS) studies on PPTA fibers showed spherical and ellipsoidal microvoids; increasing density of spherical voids and ellipsoidal voids with larger major axis resulted in lower strength [75]. Microdiffraction SAXS studies on microdissected cross sections of K29 fibers indicated nanometer scale, randomly oriented, irregular or cylindrical voids while in the skin region the voids were more elongated [28]. Microbeam SAXS studies on PPTA fibers looped to form tensile and compressive stresses on the fiber showed a fibrillated structure of cylindrical or tape-like fibrils, whose characteristic dimension increased on the tensile side and decreased on the compressive side. These results agree with small-scale fibrillation in compressed PPTA fibers, and scattering from larger cylindrical or tape-like fibrils [76] due to improved fibril packing with tension.

Further structural changes in heat-treated fibers influenced the tensile strength. XRD studies on K49 showed a decrease in the gap between the (110) and (200) diffraction peaks with increasing temperature and exposure time. This is attributed to an increase in the crystal size in the a- direction which is the direction the van der Waals interactions result in stacking of H-bonded crystalline sheets. Hence, heat treatment weakens the van der Waals interactions, which, in turn, limits load transfer between sheets and decreases the tensile strength [77,78]. Furthermore, the void size increased both laterally and longitudinally in heat-treated fibers, while smaller voids were sintered away [79]. Heat treatment of K29 at 200 °C for 15 min did not change the strength, but further heating caused a strength loss as much as 70% at 400°C [29].

The tenacity of single K29 and K49 fibers with gauge lengths 2-120 mm, was shown to increase in shorter fibers; however, data trends did not support a weakest link criterion for failure [80]. Further tests showed that as the gauge length of Kevlar® fibers decreased below <1 cm the strength was constant, which could not be explained by the weakest link theory too. Instead, it was proposed that the fibers are composed of series of 1 cm long connected links whose strength was the random variable in a Weibull distribution density function. In this model, the tensile strength is independent of fiber length for fibers shorter than 1 cm, and equal to the mean strength of the 1 cm long links [81]. To this effect, a special experimental PPTA fiber, treated to eliminate defects in the structure, showed much smaller decrease in strength with increasing gauge length with the data fitting well the proposed failure model assuming zero defect density [82]. The results suggested that the link lengths should be 1-4 cm with an average number of defects of 0-1 cm^{-1}. Finally, K49 yarn tests did not result in significant gauge length dependence of failure strain [83].

Several studies have explored the effect of strain rate on fiber strength. For quasi-static strain rates in the range 0.004-0.02 s^{-1} the mean fiber strength of K29, K49 and K149 fibers with 2.1 cm gauge length was insensitive to strain rate [84]. However, much higher strain rates applied to (<10%) pre-twisted KM2 fibers showed up to 20% increase in tensile strength at 1000 s^{-1} [85].

1.5 Objectives of this Dissertation Research

This dissertation research aimed at investigating the effect of microstructure on the deformation and failure initiation in high performance aramid fibers. The microstructure was represented by the crystalline domain orientation whose effects on the mechanical response and failure were quantified. Additional limiting factors of the mechanical strength were sought in the existence of critical defects in the fiber structure vs. a critical shear stress responsible for flaw nucleation that leads to catastrophic fiber failure.

These research objectives were undertaken using four different types of aramid fibers with different crystalline domain orientation, and mechanical properties, which were obtained from a commercial source. The distribution of crystallite orientation in each type of fiber was quantified with XRD, and was correlated with the mechanical properties measured under controlled experiments that guarantee accuracy and unbiased measurements of elastic modulus and tensile strength. The evolution of crystallite orientation during mechanical loading was investigated using 10 mm long gauge length fibers, which ensured a representative test sample in terms of variation of diameter along its length, while also guaranteeing that no flaws were introduced to the fiber during specimen preparation. The test fibers were subjected to mechanical conditioning through cyclic loading to progressively higher stresses, finally approaching the tensile strength of each aramid type. Single filament tests under monotonic loading were carried out with fiber gauge lengths in the range of 200 μm – 10 mm, thus further decreasing by one order of magnitude the smallest fiber gauge length of aramid fibers that was ever tested. These experiments aimed at assessing the existence of a critical flaw population in the fibers that obeyed the weakest link theory. Lastly, pure shear tests were carried out with a novel notched specimen design for single filaments, which was "carved out" using Focused Ion Beam (FIB) milling following a geometry that was optimized via a Finite Element Analysis (FEA) to achieve uniform shear stress and eliminate the stress singularity at notch edges. These fragile specimens were tested in tension using custom designed Microelectromechanical System (MEMS) devices.

CHAPTER 2

ORIENTATION EFFECTS ON MECHANICAL PROPERTIES OF ARAMID FIBERS

Although understanding of the processes occurring in aramid fibers at small elastic stresses is fairly thorough, the yielding and time-dependent deformation taking place in the non-linear regime of the stress-strain curves of aramid fibers are less explored. At high tensile fiber stresses, misorientation of crystalline domains promotes significant local shear, which would result in domain rotation. However, it is not clear that increased domain orientation would increase the tangent modulus because of relaxations due to crystallite sliding at high stresses. Although limited experimental data from experimental PPTA fibers have suggested increasing tensile strength with orientation [40] this correlation is not apparent in Kevlar® fibers which are the commercial counterpart of aramid fibers. Rather, Kevlar® fibers with quite different orientations have not demonstrated correspondingly different tensile strength values.

This study comes to address the question of evolution of molecular orientation with mechanical loading, starting with different initial conditions. The correspondence between as-manufactured tensile modulus and strength vs. the orientation imparted by cold drawing at different strain levels was explored in this Chapter. Towards this goal, high quality commercial aramid fibers, Kevlar®, have been utilized with different orientation distributions to deduce correlations between initial orientation and its evolution with mechanical drawing, and explore the limits controlling mechanical strength via crystalline domain orientation. Finally, the presence of strength limiting critical flaws was explored as they may be manifested in fiber gauge length size effects on tensile strength in pristine and oriented aramid fibers, reaching gauge lengths as short as 200 μm.

2.1 Materials and Experimental Methods

Experiments were conducted with individual filaments of four different grades of Kevlar® fibers manufactured with identical chemical composition by DuPont. These grades are K119, K29, KM2 and K49, which are characterized by progressively increased Young's modulus in the order listed, spanning a range in which the modulus varies by as much as 100%. Despite its challenges, testing individual fibers is of high importance in understanding microstructural effects on mechanical deformation and failure, because it is possible to compute the true fiber strength as opposed to the more common fiber bundle tests. For mechanical testing, individual Kevlar® fibers were carefully isolated from untwisted bundles, ensuring that no kinks or damage on the fiber skin were induced during sample preparation. For diameter measurements, single filaments were washed in methanol to remove residues of lubricants applied during bundle processing. This process has been shown to be very effective without resulting in surface damage [86,87]. Scanning Electron Microscopy (SEM) images of clean fiber surfaces were taken along 5 mm fiber segments to quantify the variation in diameter and obtain an accurate average value.

Clamping of high performance fibers for mechanical testing is a challenge that has been addressed in different ways depending on the nature of the fibers [88-91]. The grip compliance, including the viscoelastic adhesive or sliding at grips that rely on mechanical clamping, must be minimized or subtracted, if known and consistent between tests, in order to obtain reliable fiber stiffness measurements. Such grips tend to be stiff resulting in a stress concentration at the initial clamping point, which compromises the tensile strength [90]. For this purpose, two types of tests were performed in this study. The first utilized a two-part epoxy adhesive (Loctite Extra Time) to rigidly attach individual fibers onto a supporting frame. The stiffness of this epoxy adhesive was augmented with 10 vol% 10-20 nm silica nanoparticles, which were surface modified with epoxy groups (Skyspring Nanomaterials). After air curing the epoxy for 24 hr the supporting frames were attached to the test apparatus and were cut to set the fiber free for tensile loading. Individual fibers with 10 mm gauge length were tested at 0.01 s^{-1} strain rate to obtain the Young's modulus utilizing the stiff grips. Accurate fiber extension measurements were conducted via Digital Image Correlation (DIC) on high magnification optical images of the fiber grips that were spray painted to generate a speckle pattern. The second set of experiments were performed by bonding 1 cm long portions of fibers to supporting frames using the same epoxy adhesive as above but without reinforcing particles. The compliant adhesive aided in minimizing the stress concentration at the bonding point that originates in shrinkage during curing and mismatch between the adhesive and the fiber transverse stiffness. This type of fiber mounting ensured accurate tensile strength measurements. The Young's modulus values were correlated to the orientation distribution of crystalline domains as measured via X-Ray Diffraction from multiple bundles of fibers. After the (110) and (200) crystallographic peaks were identified, azimuthal scans were performed at (200) peak following the work by Ran et al. [25]. The orientation distribution factor, $\langle \sin^2\theta \rangle$, which is an average measure of the misorientation of crystalline domains in unloaded fibers, was calculated from the full width at half maximum (FWHM) value of a Lorentzian fit to an azimuthal scan [46]:

$$\langle \sin^2\theta \rangle = 2.1141\ \sin^2\left(\frac{FWHM}{2}\right) \tag{2.1}$$

Then, the initial elastic modulus was estimated using the orientation distribution factor, the crystal modulus along the chain axis, E_c, and the crystal shear modulus, G, as given by [47,92]:

$$\frac{1}{E} = \frac{1}{E_c} + \frac{\langle \sin^2\theta \rangle}{2G} \tag{2.2}$$

Mechanical loading of aramid fibers does not result in purely elastic deformation, as crystallites also reorient under tension. If a fiber is loaded to a given strain and subsequently unloaded, the new initial reloading stiffness reflects the mechanical response of the oriented fiber up to the strain applied in the last loading-unloading cycle. If this process is repeated to progressively higher strains, one could obtain a correlation between the increasing material orientation and the elastic properties. Similarly, the initial unloading moduli, reflect the stiffness of the fiber at the highest applied stress in each cycle, which corresponds to the most oriented material state before some orientation reversal occurs due to unloading. Towards this goal, loading-unloading tension tests with progressively increasing peak stress were conducted with 10 mm gauge length fibers at 0.01 s^{-1} strain rate. Potential history effects induced by progressive loading-unloading were evaluated using single cycle mechanical conditioning to ~80% of the failure stress, also at 0.01 s^{-1}. Finally, the time dependency of molecular re-orientation at room temperature was evaluated with monotonic tension tests at strain rates in the range 10^{-4} – 10^{-1} s^{-1} on 10 mm gauge length fibers.

The fiber strength could be limited by crystallite reorientation under tension as well as critical flaws in the fibers. The presence of the latter can be investigated via tension experiments with different fiber gauge lengths, namely if failure can be described by the weakest link theory, smaller fiber gauge lengths would result in higher tensile strengths. A comprehensive study of effect of gauge length on fiber strength using sub-millimeter specimens is currently missing due to experimental difficulties in isolation, handling and clamping individual fibers at that scale. Towards this goal, fibers with 200 µm, 1000 µm and 10,000 µm gauge lengths were tested using compliant adhesive grips to ensure accurate fiber strength measurements.

2.2 Results and Discussion

2.2.1 Effects of Orientation Distribution and Mechanical Conditioning

Figure 2.1 shows the normalized intensity vs. azimuthal angle plots measured about the (200) crystallographic peak, where a sharp peak would be expected at 0º for a fiber with perfectly oriented crystals. Instead, the intensity peaks followed a Lorentzian distribution that reflected the spread of crystallite orientations about the [200] direction. The fiber orientation distribution increased from K119 to K49 as the distribution becomes narrower.

Table 2.1 summarizes the average fiber diameter values, as measured from SEM images, the FWHM measured from fiber bundles by XRD, the measured vs. calculated

Young's modulus values for the four aramid fibers tested in this study. There is an inverse correlation between the values of FWHM and the measured modulus, therefore differences in the elastic modulus stem from crystal orientation. More importantly, this correlation is described very accurately by Equations (2.1) and (2.2): as shown in Table 2.1, the initial Young's modulus, calculated using E_c = 220 GPa [12,31,53] and G = 2 GPa [51], was in very good agreement with the measured values which confirms that this group of four fiber types has the same underlying structure and common mechanisms for load transfer determine their stiffness.

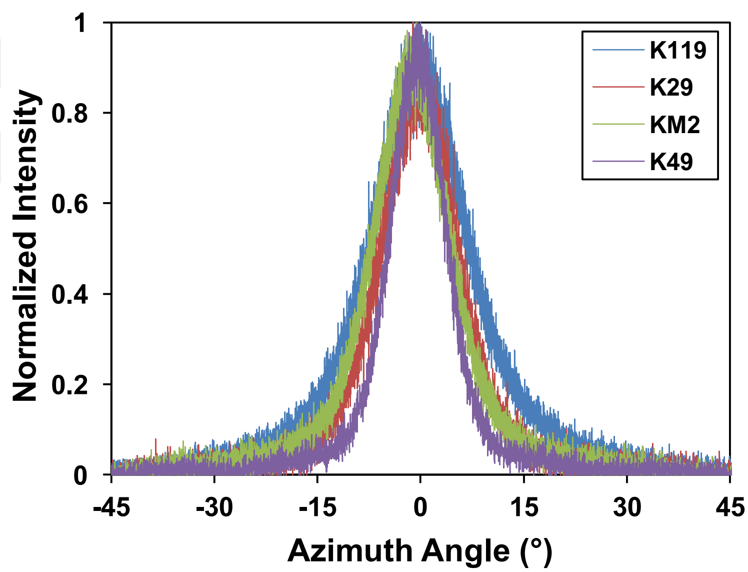

Figure 2.1 Normalized intensity vs. azimuth angle plots about (200) crystallographic peaks for four Kevlar® fibers.

Figure 2.2(a) shows the cyclic stress vs. strain curves, with progressively increasing peak stress, of the fiber type with the lowest orientation (16.7º). The very first loading-unloading cycle (1) to a peak strain of 0.85% did not show any hysteresis or permanent deformation. However, cycles 2-8 in Figure 2.2(a), reaching progressively higher peak strains, resulted in permanent strain that increased in every cycle. Each reloading stress vs. strain curve, once passing through the peak point of the last cycle, continued along the monotonic loading curve. This process of mechanical drawing results in a progressively different stress vs. strain curve which departs significantly from the behavior of a pristine fiber loaded monotonically to failure. Figure 2.2(b) provides a direct comparison between the monotonic behavior of a fiber with the lowest orientation (16.7º) and the final loading curve in Figure 2.2(a) for a filament mechanically conditioned at ~90% of the maximum tensile strength. Progressive mechanical conditioning, Figure 2.2(a), produced a bilinear response in contrast to the long non-linear transition regime seen in the stress-strain curves of pristine fibers. Furthermore, both the initial and the final tangent moduli, 64.6 GPa and 87.8 GPa, increased by 54% and 47%, respectively, demonstrating major crystallite re-orientation with mechanical stress. Unloaded PPTA fiber bundles had narrower orientation distribution than pristine bundles, suggesting permanent rotation of some of the crystalline domains [46]. Similarly, cyclic tests on K29 [68] and K49 [63,68] filaments in addition to cyclic creep tests on single K49 filaments further supported the idea of permanent rotation of domains [68]. Experiments conducted with K119 fibers oriented to 90% following the process presented in Figure 2.2(a) showed that the increased orientation and modulus, due to mechanical conditioning were retained for at least 24 hr (longer storage times were not pursued).

The monotonic stress vs. strain curves shown in Figure 2.3(a) demonstrate increasing Young's modulus and improved linearity with increasing crystallite orientation. While the mechanical response of fibers with the lowest orientation (FWHM=16.7º) deviated the most from linearity, all fiber types showed some degree of nonlinearity at 1-2% strain. The low strain segment of this "bilinear" behavior is mainly elastic as evidenced by the linear, non-hysteretic, loading-unloading segment (1) in Figure 2.2(a).

Table 2.1. Average fiber diameter, FWHM from XRD data, measured and expected Young's modulus for different grades of Kevlar® fibers.

	Diameter (µm)	Measured Young's Modulus (GPa)	Measured FWHM (°)	Calculated Young's Modulus (GPa)
K119	11.9 ± 0.4	65.6 ± 0.8	16.7	63.7
K29	12.2 ± 0.3	82.7 ± 4.4	13.5	84
KM2	10.8 ± 0.6	82.2 ± 10.9	13.5	84
K49	12.5 ± 0.4	117.3 ± 0.5	9.7	119.6

Therefore, processes occurring in that strain range are not expected to affect crystal domain orientation. The loading to higher strains, however, had very pronounced effects for all crystal domain orientations: Figure 2.3(b) shows the final loading to failure curves after a mechanical cycling as in Figure 2.2(a). Notably, the mechanical response of fibers with FWHM between 16.7º and 13.5º was linearized and converged effectively to the same curve with the same maximum tensile strength and strain. These three types of fibers were originally synthesized without post-spin heat treatment and drawing, compared to fibers with FWHM = 9.7º, Table 2.1, which were drawn at high temperature after spinning [15]. The mechanical behavior of the latter showed limited change in ultimate strain, and all four types of aramid fibers had the same tensile strength after mechanical conditioning, yet the heat-treated fibers still had the highest Young's modulus.

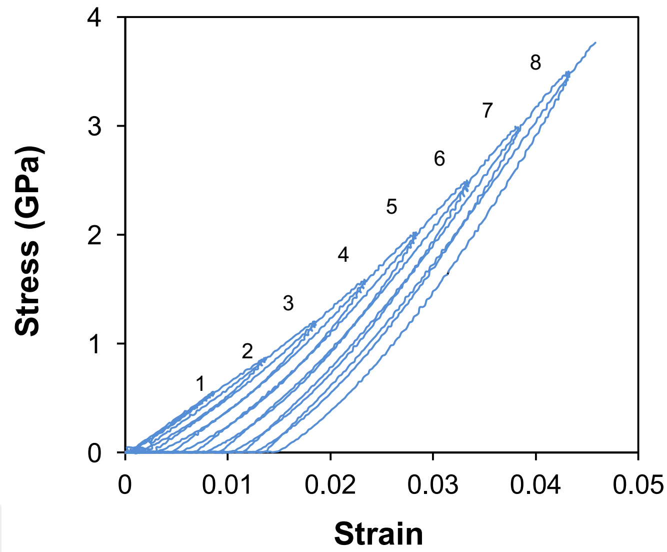

(a)

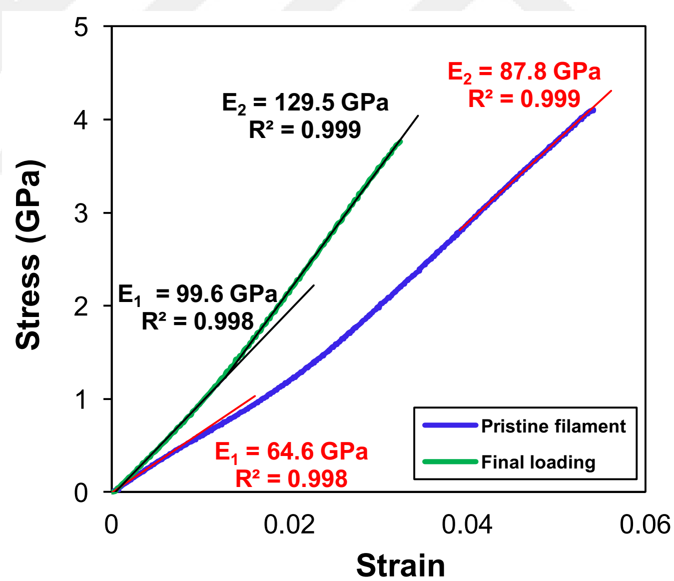

(b)

Figure 2.2 (a) Stress vs. strain curve of a filament with the lowest crystallite orientation (FWHM = 16.7º) undergoing loading-unloading at 0.01 s^{-1} with progressively increasing peak stress. **(b)** Mechanical response of a pristine filament (FWHM = 16.7º) and final loading curve of the filament in (a) showing a dramatic change in response due to mechanical conditioning to ~90% of tensile strength.

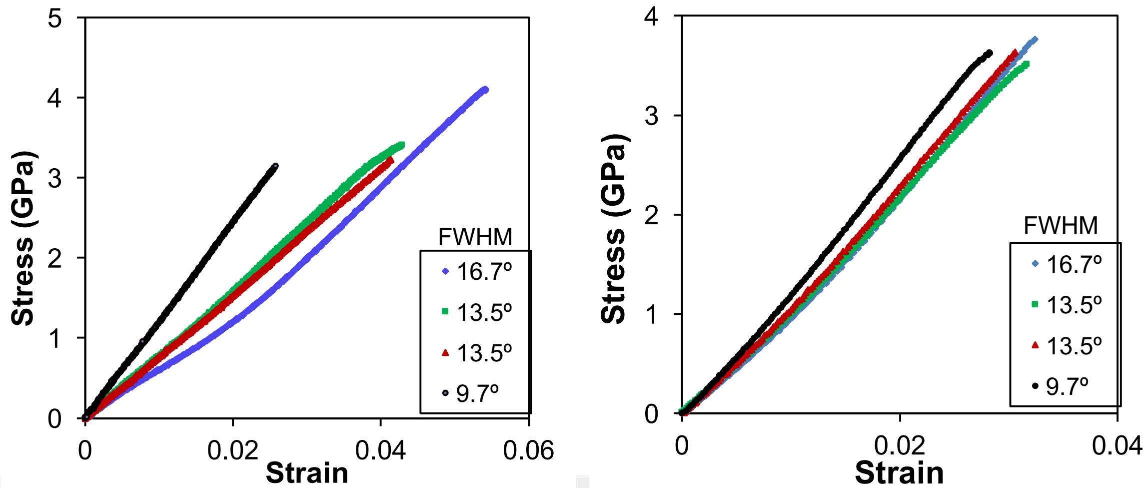

(a) **(b)**

Figure 2.3 Stress vs. strain behavior of aramid fibers with different initial crystallite orientation **(a)** under monotonic loading until failure, and **(b)** after mechanical cycling as in Figure 2.2(a), followed by complete unloading and monotonic loading to failure. In both figures, the FWHM is the value of the pristine fibers.

The loading and unloading moduli provide indirect information about the evolution of orientation distribution with increasing peak strain during mechanical conditioning. As shown in Figure 2.4(a), the initial reloading modulus was unaffected by mechanical cycling up to 2% strain. In fibers with FWHM 16.7º – 13.5º, all crystal domain re-orientation took place between 2-3% applied strain and the initial reloading elastic modulus of all three fiber grades converged to 100 GPa. On the other hand, the elastic modulus of fibers with initial FWHM = 9.7º, which were subjected to post-spin heat treatment, remained unaffected as 120±1 GPa.

Notably the maximum possible orientation in all four types of aramid fibers tested in this work corresponds to FWHM values much smaller than 9.7º. As shown in Figure 2.4(b), the unloading stiffness at 90% of the maximum tensile strength reached the values of 170 GPa, 165 GPa, 160 GPa, and 159 GPa, for K49, KM2, K29, and K119, respectively. Furthermore, contrary to the stable initial reloading modulus with increasing cyclic peak stress for the highest oriented fibers (FWHM=9.7º), mechanical conditioning caused a linear increase in the initial unloading modulus from 139 GPa to 170 GPa. Thus, even for high temperature drawn aramid fibers, further significant increase in crystalline domain orientation is possible, but is reversed upon unloading. Thus, near the peak stress, the fiber stiffness is the closest to the theoretical modulus of 220 GPa for a PPTA crystal. By means of Equation (2.2) the unloading modulus of 170 GPa corresponds to FWHM=5.8°, compared to 9.7° for the pristine K49 fiber. The contraction in orientation distribution was more significant, from 16.7° to 6.6°, for K119 fibers although FWHM increased to 11.6º upon complete unloading. Notably, in none of the four fiber types the increase in crystallite orientation was accompanied by concomitant increase in tensile strength: As will be shown later, for all four types of aramid fibers, the tensile strength of monotonically loaded filaments was virtually identical to the mechanically cycled counterparts. Thus, the mechanical stiffness and crystalline domain orientation are decoupled from the tensile strength, which implies that the ultimate tensile strength is controlled either by pre-existing critical flaws whose size is independent of processing and applied strain, or critical flaws that nucleate near the tensile strength of 3.5-4 GPa which was common for all aramid fibers tested in this work.

It remains to show that the actual crystallite orientation upon complete unloading is the same as that calculated using the reloading moduli values. To this effect, Figure 2.4(c) compares the XRD-measured FWHM values of unloaded fiber bundles, which were preconditioned at different peak strain values, with those estimated via Equation (2.2), with the reloading modulus reported in Figure 2.4(a) as the input. The agreement between the estimated and measured orientation verifies the close correlation between the crystalline domain orientation and the measured instantaneous modulus. The constant reloading modulus of as-spun filaments loaded up to ~2% strain, Figure 2.4(a), is in agreement with the virtually unaffected orientation distribution upon unloading in the same strain regime. For preconditioning strain values larger than 2% the increased crystallite orientation after unloading was that expected from Equation (2.2) for the measured reloading modulus.

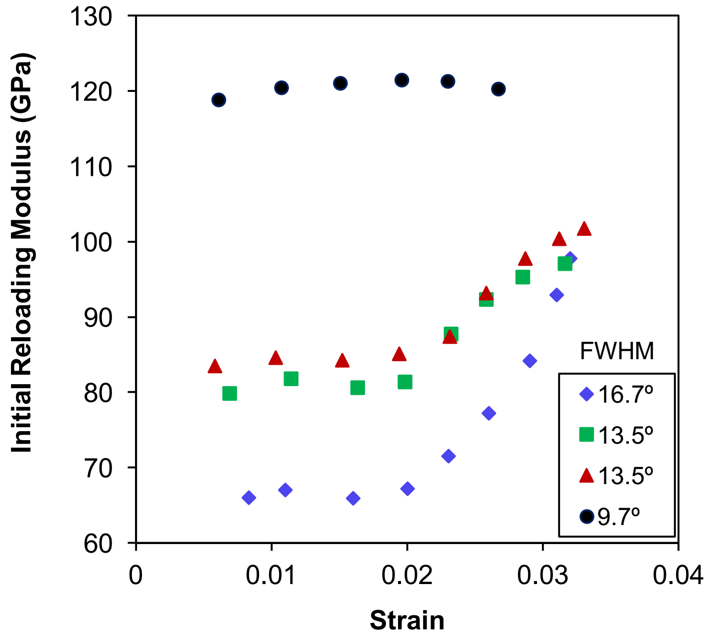

(a)

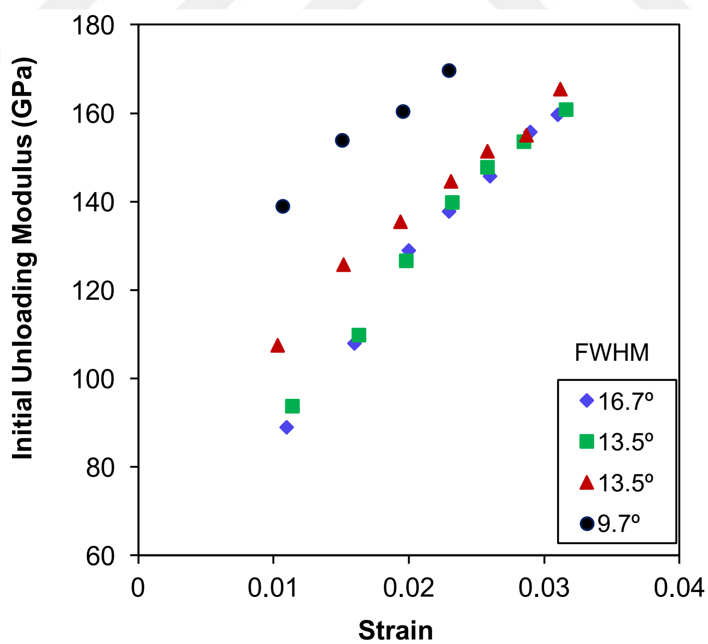

(b)

Figure 2.4 (cont.)

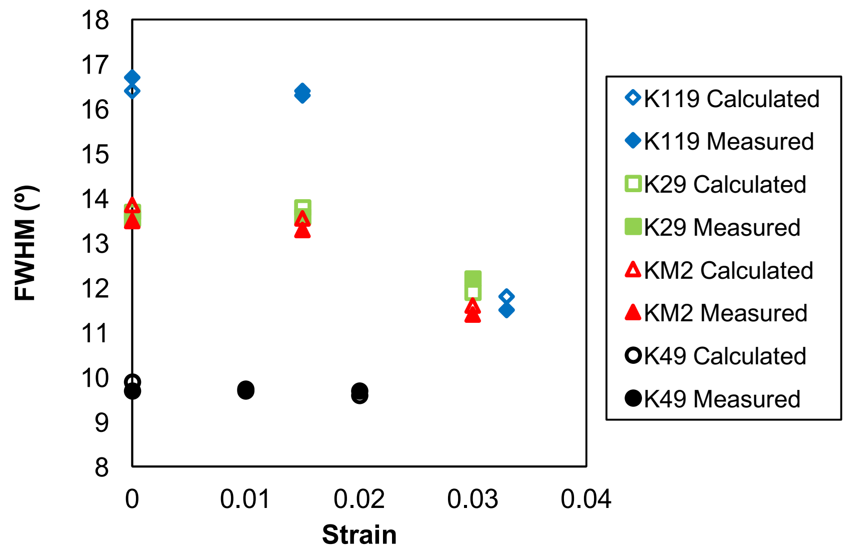

(c)

Figure 2.4 Initial **(a)** reloading, and **(b)** unloading moduli with progressively increasing preconditioning strain of aramid filaments with different initial orientation. **(c)** Comparison of measured FWHM values of unloaded fiber bundles (filled symbols), preconditioned at different strain values, with calculated FWHM values (open symbols) using the reloading moduli in (a).

It should be noted that the final permanent crystallite orientation, as reflected in the value of the initial reloading modulus, and the highest crystallite orientation, as reflected in the value of the initial unloading modulus, depend only on the maximum applied stress and are independent of the number of loading-unloading cycles. To this effect, Figure 2.5 shows a comparison of the reloading stress-strain curve (open symbols) after cycling a K119 fiber up to ~80% of the monotonic tensile strength using the routine shown in Figure 2.2(a), with the reloading curve after only one cycle to 80% of the fiber tensile strength (filled symbols). The two approaches to mechanical conditioning resulted to the same initial moduli (~93.5 GPa) and final moduli (~124 GPa) which supports the argument that the outcome of mechanical drawing depends only on the peak stress and is independent of the details of the loading history.

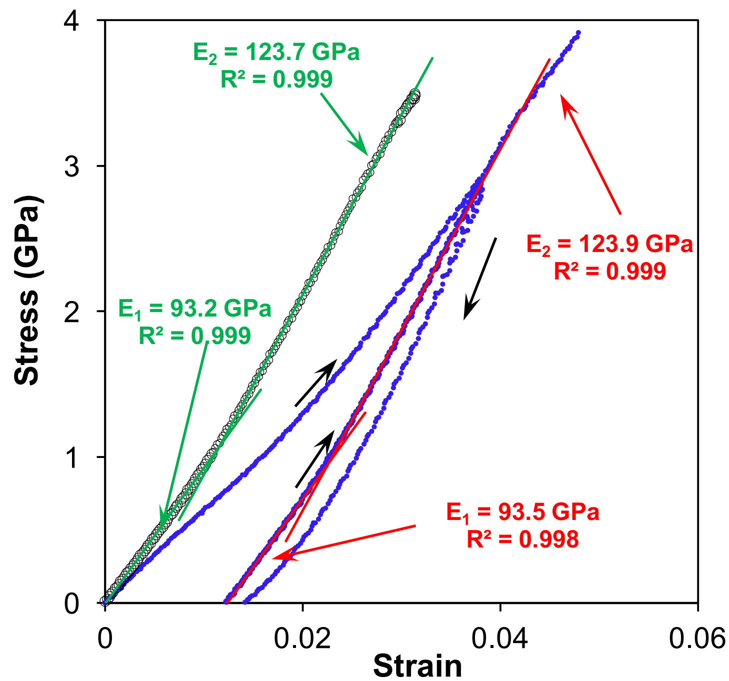

Figure 2.5 Stress vs. strain curves of two filaments with the lowest initial orientation (FWHM=16.7º): (open symbols): loading curve #8 in Figure 2.2(a). (filled symbols): a fiber loaded monotonically to ~80% of the ultimate tensile strength, unloaded and reloaded to failure.

2.2.2 Effect of Strain Rate on Orientation Evolution

The process of crystalline domain orientation entails severing and reforming van der Waals bonds, a process that is thermally activated and, as such, subject to rate effects. This rate dependency was tested within the quasi-static regime at four strain rates ranging from 10^{-4} to 0.3 s^{-1}. Using the elastic stiffness as a measure of crystalline domain orientation in individual filaments, 10 mm long aramid fibers of the lowest (16.7º) and the highest FWHM (9.7º) were tested, Table 2.1. As shown in Figure 2.6(a,b), there is clear sensitivity to strain rate at strains larger than 2%, which, according to Figure 2.4(a), is also the strain threshold to impart permanent crystallite orientation in the fibers.

Specifically, increasing strain rate has suppressed the hardening behavior, a finding not reported before for individual aramid filaments, because the majority of tests with aramid fibers in literature have been conducted with fiber bundles. At strain rates of 0.2-0.3 s^{-1} hardening is completely suppressed resulting in linear behavior until failure without affecting the fiber strength. This effect is much pronounced for the fibers with the lowest initial crystalline domain orientation, Figure 2.6(a), and of less importance for fibers with the highest initial crystallite orientation, Figure 2.6(b). These results show that the crystalline domain orientation process, which is based on breaking and reforming van der Waals bonds, is viscous in nature and is limited by the applied strain rate: slower strain rates accommodate the cascade of sacrificial bond rearrangements, thus yielding higher orientation and modulus before failure. High strain rates (>0.2 s^{-1}) do not provide sufficient time to crystallites to orient with the fiber axis, hence retaining the initially linear stress-strain behavior until failure, Figure 2.6(a,b). From a processing view point, since the fiber tensile strength is not affected by the strain rate (for the limited rates tested here), mechanical conditioning to improve crystalline domain orientation could be conducted at slower strain rates and lower peak strains compared to faster strain rates: Figure 2.7 shows such an example of a 10-mm long filament of the lowest orientation (FWHM=16.7º) which was conditioned to 90% of the tensile strength at the (faster) strain rate of 10^{-2} s^{-1} but to 80% at the (slower) strain rate of 10^{-4} s^{-1}, yet resulting in the same final loading curves with practically the same moduli at low and high stress.

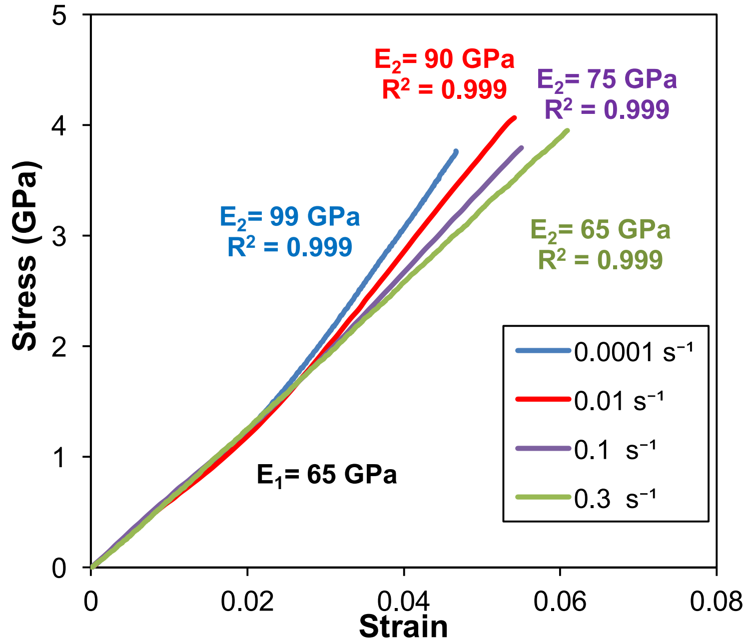

(a)

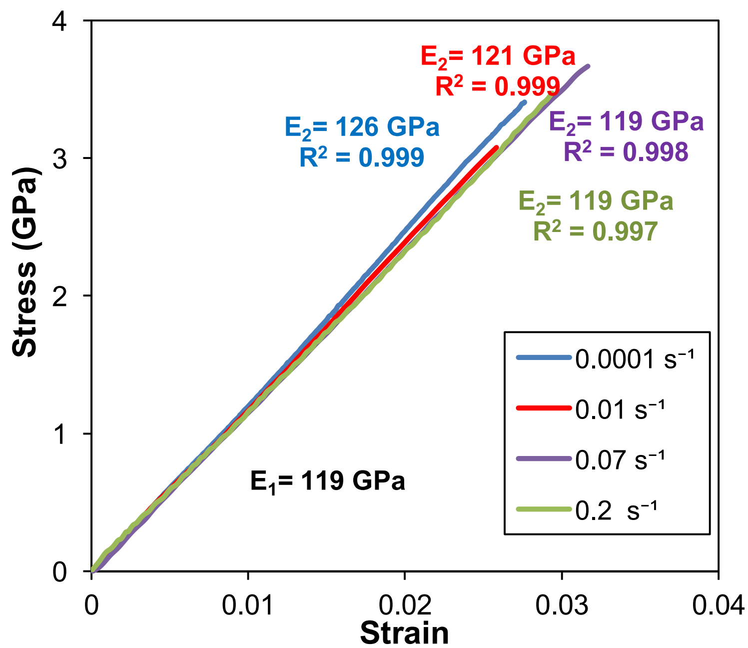

(b)

Figure 2.6 Effect of strain rate on the mechanical response of aramid fibers with **(a)** the lowest (FWHM=16.7º), and **(b)** the highest (FWHM=9.7º) crystalline domain orientation of the fibers listed in Table 2.1.

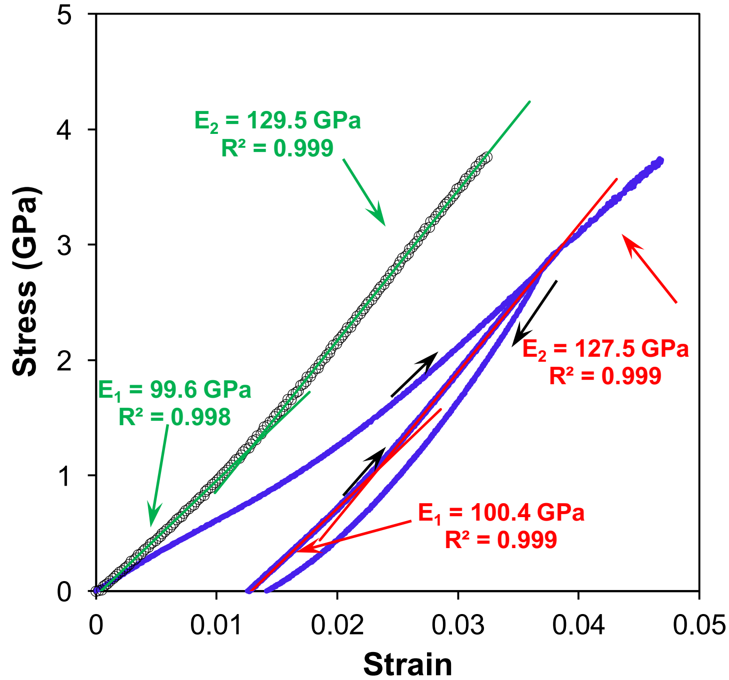

Figure 2.7 Mechanical response of a pre-conditioned K119 fiber up to 90% of the tensile strength at strain rate 10^{-2} s^{-1} (open symbols), vs. loading-unloading to 80% of the tensile strength and final reloading at 10^{-4} s^{-1} (filled symbols). The two approaches resulted in practically the same final loading curves up to each conditioning strain.

2.2.3 Effect of Mechanical Conditioning on Tensile Strength

Contrary to pronounced improvements in mechanical stiffness with crystalline domain orientation, the average tensile strength of 10 mm gauge length filaments of all aramid fiber types did not correlate with the orientation distribution. Rather, the tensile strength was unaffected by mechanical cycling, as deduced from the data in Table 2.2. The tensile strength of the initially strongest fibers (by less than 0.5 GPa compared to the rest), which had the broadest orientation distribution, (FWHM=16.7º) remained practically unchanged after mechanical conditioning. Increased orientation is expected to increase the load carrying capacity due to higher intercrystallite load transfer efficiency. While mechanical conditioning did not result in increased tensile strength, it did not have an adverse effect on tensile strength either. Early studies with PPTA fibers [67] subjected to different spinning and heat treatment conditions showed that higher orientation could lead not only to higher elastic modulus but also higher strength, for fibers with initial moduli lower than 65 GPa. For moduli values between 65 GPa and 150 GPa the tensile strength was between 2.5 - 4 GPa, and decreased sharply for fibers with initial moduli higher than 150 GPa. The results of the present study show that although the initial unloading modulus of all fiber types reached 160-170 GPa after high stress conditioning, Figure 2.4(b), the tensile strength did not change from that of pristine fibers. This result, along with the strain rate insensitivity established in the previous Section, point to the possibility for preexisting surface or volumetric flaws in the fiber structure that are unaffected by crystalline domain orientation and limit the tensile strength of this class of fibers.

Table 2.2. Effect of orientation and mechanical conditioning on the tensile strength of 10 mm long Kevlar® filaments.

Fiber Type	Measured FWHM (°)	Pristine fiber strength (GPa)	Conditioned fiber strength (GPa)
K119	16.7	3.97 ± 0.31	4.09 ± 0.31
K29	13.5	3.46 ± 0.3	3.41 ± 0.2
KM2	13.5	3.76 ± 0.19	3.87 ± 0.33
K49	9.7	3.57 ± 0.34	3.79 ± 0.11

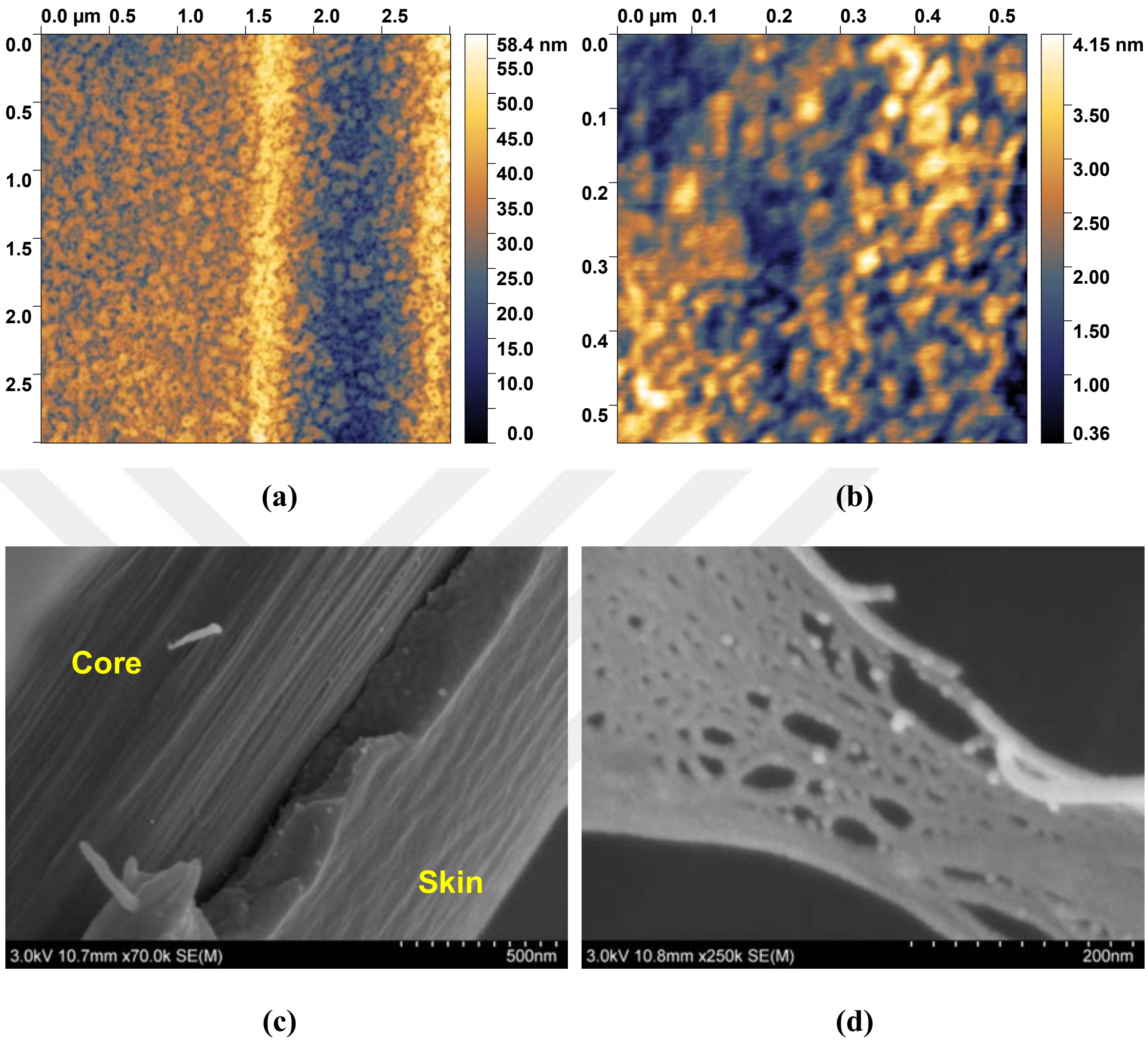

Figure 2.8 (a) AFM topography images of the skin surface of **(a)** K49, and **(b)** KM2 fibers. **(c)** Skin-core separation in a KM2 fiber. **(d)** Fibrillated sheet of microfibril crystals from the core of a KM2 fiber, showing a consistent microfibril diameter of 5 nm. The bright spots in the fibrillar web are the crystal ends.

In terms of surface flaws, the outer surface of carefully isolated aramid fibers was examined via high resolution AFM, as prior AFM studies have identified a variety of defect structures on the surface of aramid fibers, which could be potential failure sites [93]. The AFM images showed only long longitudinal ridges, Figure 2.8(a) which do not represent stress concentrations, while the rest of the fiber surface was very smooth with an RMS roughness of as low as 0.6 nm for KM2, as computed from Figure 2.8(b). Notably, none of the AFM images revealed a fibrillar structure on the outer fiber surface, which is consistent with the current notion that the fiber skin is not crystalline [15,94]. However, there is clear differentiation between the outer fiber skin of ~200 nm thickness and the inner fiber, forming an interface of relative weak cohesion which is prone to separation, as can be seen in Figure 2.8(c). The fibrillar structure is a distinct feature of the fiber core, which is comprised of microfibrils with an average diameter of 5 nm, Figure 2.8(d), and lengths of the order of 200 nm [11,26]. Extensive SEM imaging of split KM2 fibers has shown that the ~5 nm building block microfibrils are the only persistent length scale in the hierarchy of the fiber structure; larger diameter fibrils observed in ruptured or kinked aramid fibers are merely the result of dynamic fracture. Thus, failure initiation should be sought in flaws relating to fiber features with length scales that are larger than the microfibril diameter.

2.2.4 Scaling of Tensile Strength with Fiber Gauge Length

The lack of correlation between crystallite orientation distribution and tensile strength prompts the investigation of pre-existing flaws. The latter would have a distribution of length scales which would correlate with the specimen size, thus resulting in gauge size effects. Known defects are isolated chain ends, side groups and interstitials at the molecular level, while voids and clustered chain ends may form weak planes at the fibrillar scale [9]. Small-angle X-ray scattering (SAXS) studies on PPTA fibers have shown spherical and ellipsoidal microvoids: increased density of spherical voids and a longer major axis of ellipsoidal voids could result in lower strength [75]. Microdiffraction SAXS studies with K29 fibers pointed to nanometer-scale, randomly oriented, irregular, cylindrical, and elongated voids [28]. Notably, heat treatment did not annihilate these flaws or produced stronger fibers: XRD studies of fibers with the tightest orientation distribution (FWHM=9.7º) [77,78] have suggested an increase in the crystal size in the direction in which van der Waals interactions result in stacking of H-bonded crystal sheets. This weakens the van der Waals interactions and limits the load transfer between sheets, hence decreasing the tensile strength.

Given the variety of defects identified in prior XRD studies, tension tests with individual aramid filaments of different gauge lengths could provide evidence for a specimen size effect on tensile strength. Prior experiments by Lim et. al [95] on aramid fibers with gauge lengths 2.5 - 250 mm have yielded a very modest change in tensile strength with gauge length, which increased by 10-15% for small gauge lengths (2.5 mm). However, the data at small gauge lengths were inconclusive because of the large data scatter. On the other hand, tests with single K29 and K49 fibers that were 2-120 mm long [80], have shown increasing tenacity with decreasing gauge length. These results did not fit a Weibull-type flaw distribution that would support a weakest link type of failure. Finally, tests by Knoff [81] have shown constant strength for fiber lengths below 10 mm. The differences between prior studies must also be understood by considering the difficulties in specimen preparation and testing: isolation of long filaments from bundles with hundreds of filaments is not without risk of inducing surface defects and kinks. At the other extreme, test specimens with dimensions of the order of 2 mm require precision cutting and clamping, while very small gauge lengths indirectly reduce the risk of handling defects. Thus, the aforementioned considerations could lead to preparation-of-specimen size effects. The experiments in this work focused on extending the range of prior studies by a factor of 10 towards smaller gauge lengths. Figure 2.9 summarizes the tensile strength values for the four aramid fibers described in Table 1, for gauge lengths 200 μm, 1 mm, and 10 mm that correspond approximately to 20-1000 fiber length-to-diameter ratios. The results are also compared to the tensile strength measured from 10-mm long fibers conditioned to ~80% of the fiber tensile strength. Two conclusions emerge from the plots: (a) within one standard deviation, the tensile strength of all fiber types is independent of gauge length down to 200-μm filaments, and (b) mechanical conditioning does not affect the fiber tensile strength. The standard deviation could account for variations of the fiber diameter about the mean value, which is significant as shown in Table 2.1.

This gauge length insensitivity suggests that before any existing defects could initiate failure, new catastrophic flaws may nucleate at the high tensile stress of ~4 GPa either in the fiber core or the skin-core interface. Since the aforementioned nanoscopic pre-existing flaws in the fiber core are too small to directly initiate failure, it is deduced that a likely site for failure initiation is the fiber skin-core interface. The skin has a distinctly different structure, Figure 2.8(c), compared to the fibrillar core, and, higher stiffness. Isostrain conditions at high extensional stresses (i.e. ~4 GPa) could generate major interfacial shear stresses that cause skin-core debonding, signs of which are shown in Figure 2.8(c). New evidence towards this argument is provided by the distinctly different mode of failure of the 200 μm long filaments, which demonstrated a sword-in-sheath type of failure, as illustrated in Figure 2.10(a-c). As shown in the time-lapse optical images in Figure 2.10(a), failure occurred by skin fracture followed by "extrusion" of the core from the skin, which propagated in the entire length of the fiber including the segment that was bonded with a compliant adhesive for clamping purposes. As a result, a core (sword) with a length of 5-10 times the 200-μm gauge length was extruded from the fiber inside the adhesive, Figure 2.10(a,d). The peeled skin in the gauge section revealed the fine fibrillar core structure, Figure 2.10 (c,d), compared to the smooth skin. Although the outer fiber skin surface has no fibrillar structure, Figure 2.8(a-c), the separated skin from the core had an inner fibrillar surface, Figure 2.10(b,c), which may imply that failure occurs not at the interface but inside the fibrillar fiber core near the skin-core interface. Thus, the stress-controlled failure process is associated with shear failure initiation at the fiber core-skin interface, where significant interfacial shear and potentially triaxial stresses develop at high axial forces. While long filaments result in dramatic fibrillation upon tensile failure, the very short, 200-μm long, filaments reduced the total elastic strain energy stored in the fiber during testing, and permitted the observation of failure initiation. This sword-in-sheath type of failure was not observed for the 1 mm and 10 mm long filaments tested under the exact same conditions as the 200 μm fibers.

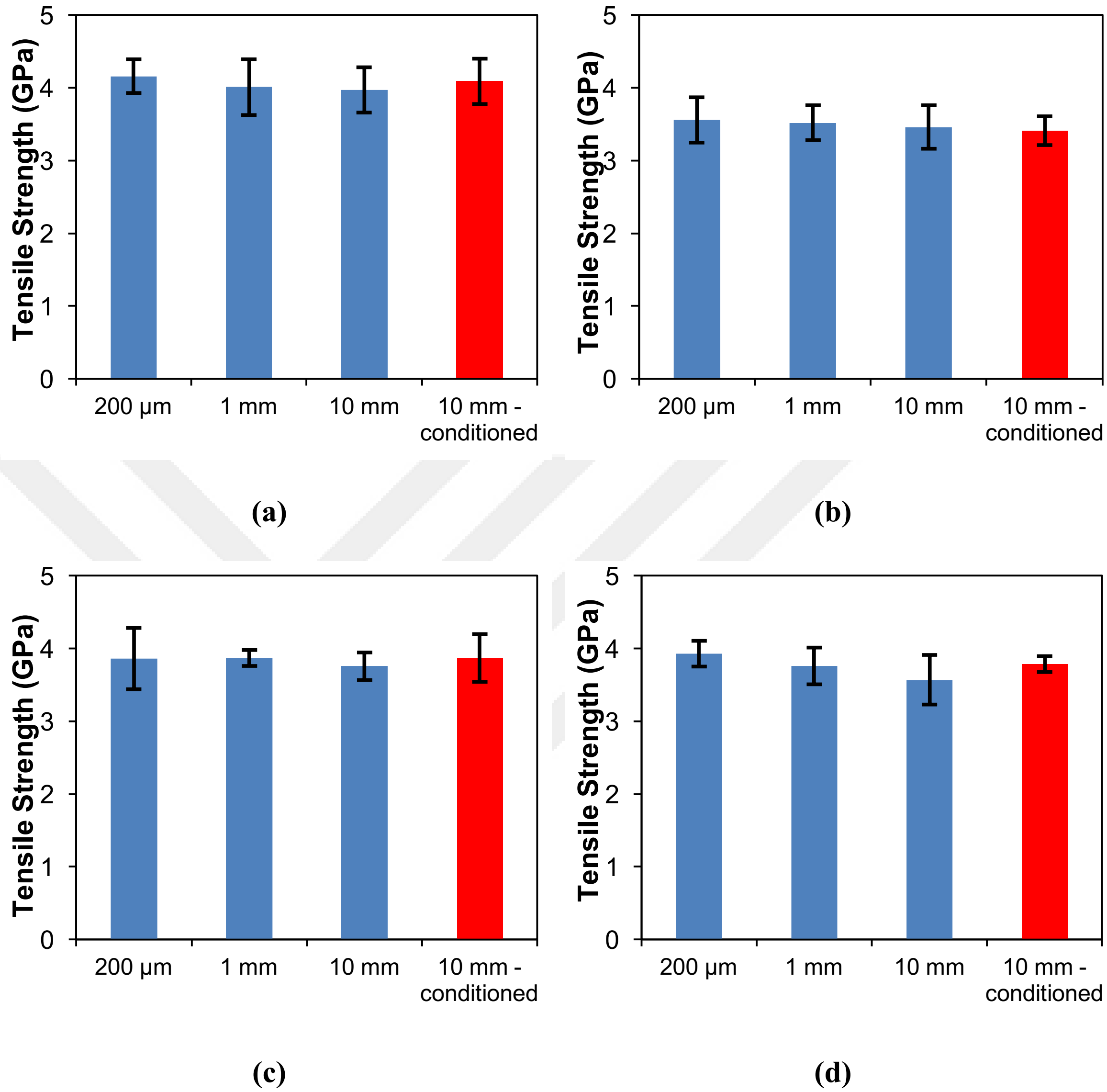

Figure 2.9 Tensile strength of individual **(a)** K119, **(b)** K29, **(c)** KM2 and **(d)** K49 fibers with gauge lengths 200-10,000 µm, and comparison with 10 mm fibers conditioned to ~80% of tensile strength before tensile testing.

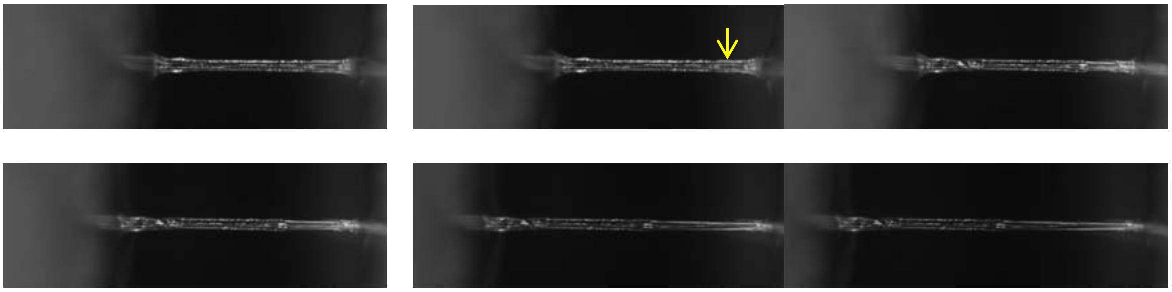

(a)

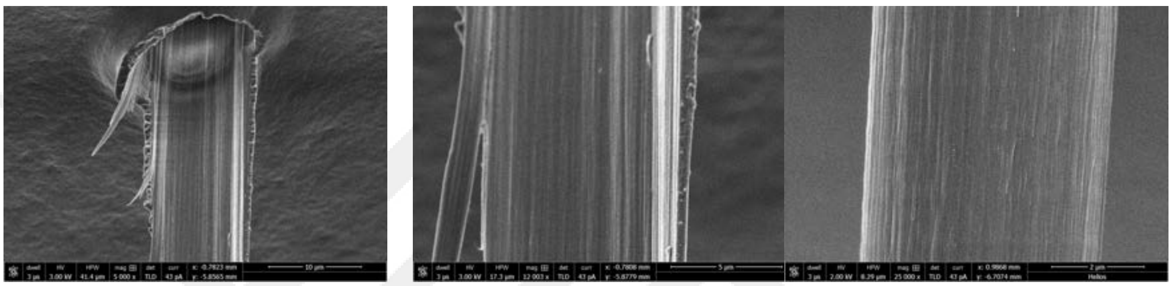

(b) **(c)** **(d)**

Figure 2.10 (a) Time lapse optical images showing failure initiation and propagation at the skin-core interface of a short gauge length K29 fiber (the initial fiber length is 200 µm). The arrow points to a crack that formed in the skin 500 ms before failure initiation and extrusion of the fiber core as pointed out in subsequent images. SEM images showing **(b,c)** the inner surface of the separated skin of a K29 fiber, and **(d)** the extruded core of a KM2 fiber.

2.3 Conclusions

In this study, mechanical stress was shown to improve crystalline domain orientation, increase both the initial and the final Young's moduli, and linearize the stress vs. strain curves of aramid fibers with different initial crystalline domain orientation. These effects were retained upon complete unloading and were shown to be independent of the loading path. Different types of aramid fibers with FWHM values of 16.7º and 13.5º converged to the same tensile behavior when conditioned to ~90% of their respective tensile strength. Independently of the initial Young's modulus of pristine filaments, all fibers reached the same orientation distribution at the instant of failure, corresponding to FWHM=6.6º, as computed from the measured value of the unloading modulus. A slightly smaller FWHM value of 5.7º was possible only for aramid filaments that were hot drawn after spinning with initial FWHM=9.7º. However, mechanical conditioning up to ~90% did not change initial modulus of the latter, and both as-spun and heat-treated aramid fibers attained approximately the same unloading modulus of 160-170 GPa, namely the same maximum orientation of crystalline domains. Orientation of crystallites during mechanical conditioning was shown to be a rate dependent process without nucleation of new flaws, which is consistent with the process of breaking and reforming van der Waals bonds that form the crystal structure of aramids. The tensile strength was also insensitive to fiber gauge length for filaments as short as 200 μm, namely failure does not follow the weakest link theory, and therefore, may not depend on a pre-existing distribution of voids. Instead, SEM imaging has shown clear structural differentiation between the fiber core and the skin which separated upon fiber failure in all short filament tests (200 μm) in a sword-in-sheath fashion instead of the classical fibrillar rupture of long filaments. This new experimental finding points to the role of interfacial shear stress between the crystalline core and the highly aligned fiber skin as the factor limiting the tensile strength of this class of aramid fibers.

CHAPTER 3

SHEAR STRENGTH OF ARAMID FIBERS

Although prior studies, as summarized in Chapter 1, have focused on the tensile behavior of aramid yarns or single filaments, only a few have concentrated on estimates of the shear strength [56,61,85]. In those studies, shear stress was imposed by twisting individual aramid filaments. Although challenging, due to inherent difficulties in sample preparation and testing at the micrometer scale, the accurate and direct measurement of shear strength of single aramid filaments could enable modeling and prediction of the limits on crystallite reorientation under tensile load, following the hypothesis that further reorientation by means of shear deformation and sliding of crystallites could result in defect nucleation and fiber failure. Moreover, proper understanding of the effect of shear stress on the tensile fiber strength may guide further computational and synthesis studies on liquid crystal-based fibrous materials with stronger secondary bonded interactions between crystallites. Motivated by the aforementioned hypothesis, this Chapter focuses on the development of novel experiments for the measurement of the in-plane shear strength, τ_{zr}, of individual polymer fibers. Using this method, the shear strength of individual K119 filaments, with 4 GPa tensile strength and 66 GPa Young's modulus has been measured and reported.

3.1 Background on Shear Testing of Materials

Accurate shear testing of materials requires careful consideration of the stress distribution in the test specimen in order to minimize, if not completely eliminate, the tensile and compressive stresses in the region of interest while maintaining the shear stress as uniform as possible. Over the years novel specimen geometries, such as the ones by Iosipescu [96,97], Figure 3.1(a), and Miyauchi [98-100], Figure 3.1(b), have been utilized and further refined. These designs require special fixtures and work well with 2D, plate-like specimens. Standardized specimen geometries following the ASTM standard B831 [101], Figure 3.2(a), and shear compression specimens [102,103], Figure 3.2(b), generate shear zones in a specimen under tensile or compressive load, which makes efficient use of universal testing frames or high strain rate apparatuses such as Kolsky bars. As a result, several studies have focused on the analysis of the stress distribution in the slotted shear specimen to ensure shear dominant deformation and shear strain uniformity by inserting rounded [104-109] or eccentric notches [110,111]. Thinning down the shear zone in the out-of-plane direction minimizes the inherent problem of shear plane rotation due to the asymmetry in the slotted shear specimens [112-116], while specimens modified to attach to a specialized holder can also restrict rotation [117].

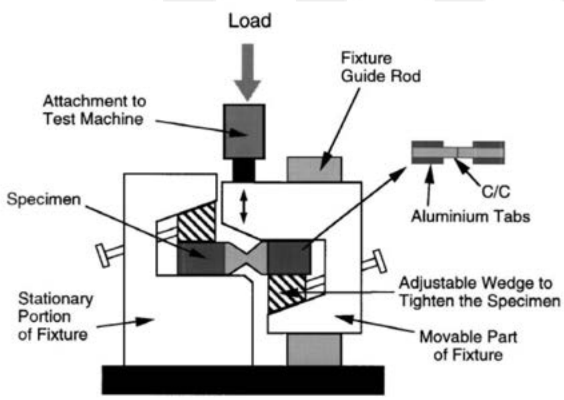

(a)

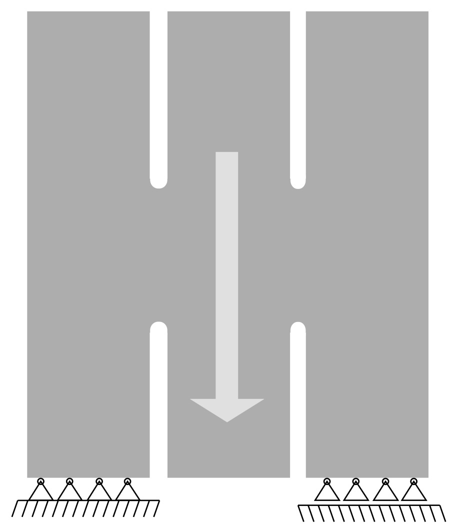

(b)

Figure 3.1(a) Iosipescu specimen with a V notch tested using a specialized fixture [118]. **(b)** Miyauchi shear test specimen with two parallel shear zones [99]. Figures reprinted with permission from Elsevier.

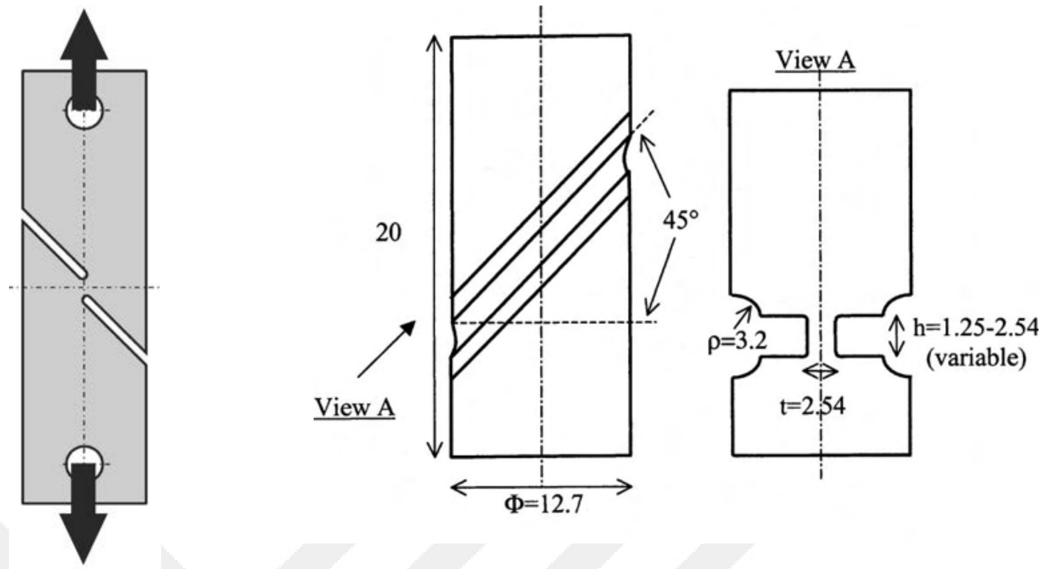

(a) **(b)**

Figure 3.2 (a) Slotted shear test specimen based on ASTM standard B831 [99]. **(b)** Original shear compression specimen developed by Rittel and co-workers [102,103]. Figures reprinted with permission from Elsevier.

Recently, shear loading of aramid filaments has been reported with the objective to reveal the inner structure rather than measure the force at shear failure, which was proven to be very small to measure [119]. Figure 3.3(a) shows a symmetric double notch specimen used in the aforementioned study, which resembles a Miyauchi specimen with two symmetric shear planes, and Figure 3.3(b) shows an asymmetric slotted shear type specimen [94], both obtained by inserting notches into a single Kevlar® KM2 fiber by using a Focused Ion Beam (FIB). The 90° asymmetric slotted shear specimen in Figure 3.3(b) served the purpose of revealing the inner fibrillar structure, therefore issues arising from the use of two normal cuts, such as significant rotation and normal stresses around the shear zone, were not considered. With this technique, the authors obtained cleaved internal surfaces better than those that can be obtained with microtoming, which enabled the observation of a fibrillar structure via AFM modulus mapping.

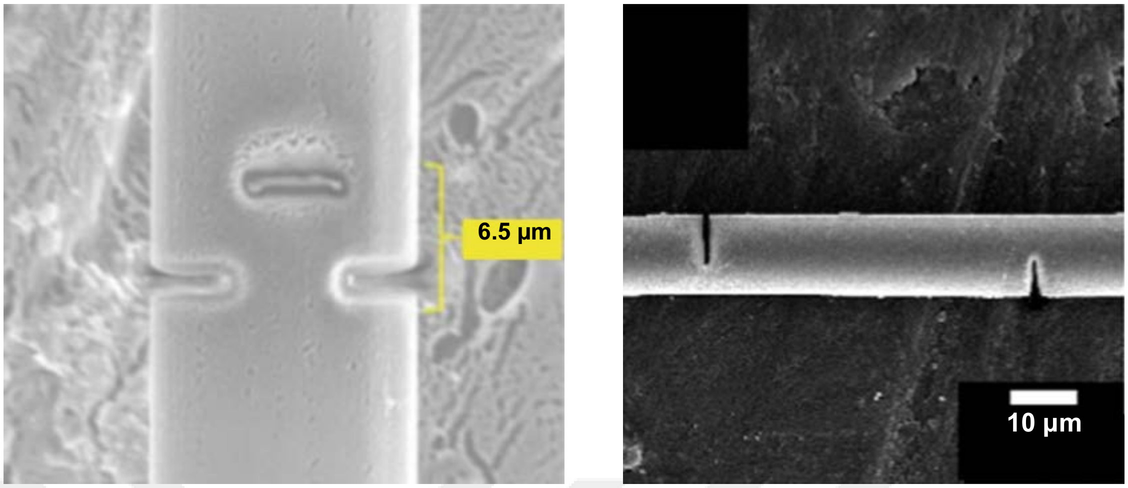

(a) (b)

Figure 3.3 (a) Symmetric double edge-notched specimen [119]. Reprinted with permission from Springer and **(b)** asymmetric slotted shear type specimen machined using a FIB on a single KM2 filament [94]. Reprinted with permission from Elsevier.

3.2 Experimental Methods

3.2.1 Specimen Design for Shear Strength Measurements

The symmetric double edge-notched specimen introduced in the previous Section was evaluated first in this dissertation research and an analysis and preliminary experiments were performed. A Finite Element Analysis (FEA) was utilized to determine the spacing between the notches and the central slit, and the size of the notches, in the specimen geometry shown meshed in Figure 3.4(a,b). The FE mesh consisted of 8-node linear brick elements with increasing mesh density around the shear zone, as shown in Figure 3.4(b). The elastic constants of the transversely isotropic fiber model were adopted from Cheng et al. [120] for a KM2 fiber, and are summarized in Table 3.1: E_1 and E_2 are the transverse elastic moduli, G_{13} and G_{23} are the shear moduli for the transverse-longitudinal plane, ν_{12} is the Poisson's ratio for the transverse-transverse plane, and ν_{31} is the Poisson's ratio for the longitudinal-transverse plane. The elastic modulus along the fiber axis, E_3, for KM2 fibers was measured in this work and reported in Chapter 2. Figure 3.4(c) shows the shear stress profile, normalized by the average shear stress, along a line passing through the center of the shear plane. The stress singularity, which could not be modeled by brick elements, resulted in spikes of shear stress at the notch edges. In practice, the notch edges do not form perfect 90° angles, and the rounded edges alleviate the stress singularity, albeit still generate a high stress concentration that will initiate early shear failure and would limit our ability to calculate the shear strength. Therefore, this specimen geometry is ineffective in determining the true fiber shear strength.

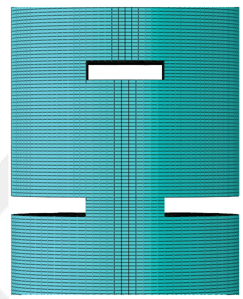

(a) **(b)**

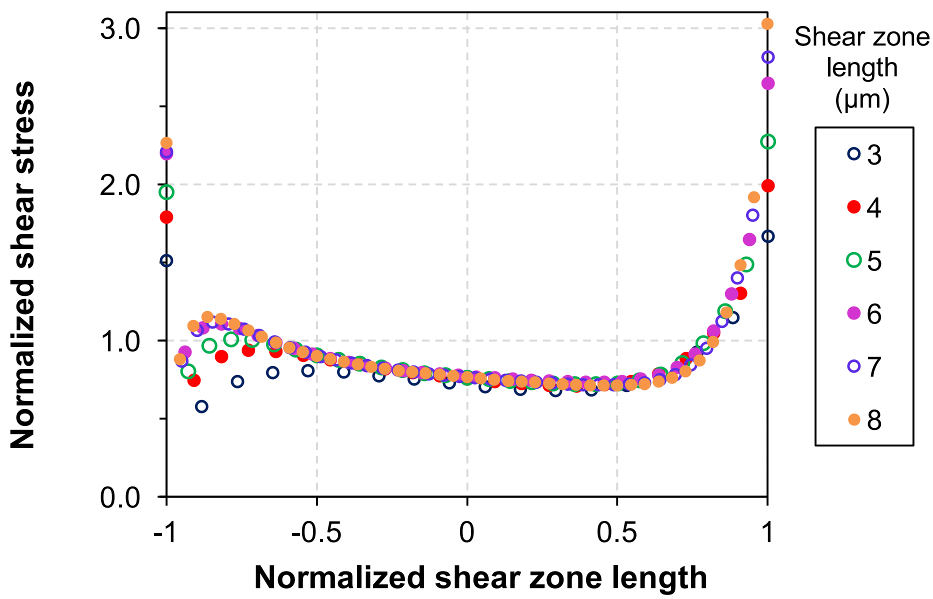

(c)

Figure 3.4 (a) FE model of symmetric double notch specimen. **(b)** Detail of the mesh in the shear zone. **(c)** Shear stress profile along a line passing through the center of the shear plane, normalized by average shear stress. Note the stress singularity at the notch edges at ±1.

Table 3.1. Elastic constants used in the transversely isotropic FE fiber model, derived for a KM2 fiber by Cheng et al. [120], except for E_3 that was measured in this work.

E_1, E_2 (GPa)	E_3 (GPa)	G_{13}, G_{23} (GPa)	ν_{12}	ν_{31}
1.34	82	24.4	0.24	0.6

Instead, the stress profile at the tip of the edge notches can be shaped, and potentially controlled, by changing the local angle at the notch tip corner by introducing semicircular cuts, Figure 3.5(a,b). With this modification the shear stress profile vanishes at the notch tip edges and is uniform in approximately half of the shear zone length for a 3-μm shear zone length, as shown in Figure 3.5(c). Figure 3.6(a) shows SEM images of a K49 fiber, attached using a Devcon two-part epoxy to a Microelectromechanical System (MEMS) type device designed for small scale experiments with individual fibers. Figure 3.6(b) shows the same fiber after the edge notches, pointed by arrows, were created via FIB. The use of a FIB results in some ion beam damage around the central slit. Figure 3.6(c) is a post-mortem view of the matching specimen sides. As shown, during shear deformation and failure, fibrils were extracted from the matching surface at the notch tip edges. The very small width of the notches, created within the limitations of a FIB, as well as the non-circular fiber cross-section, resulted in inevitable asymmetric notches and, thus, a tensile stress component that could have contributed to the extruded fibrils. Moreover, Ga^+ ions scatter inside the deep and narrow central slit as ion milling is progressing, causing damage to the side walls of the central slit, as pointed by the arrow in Figure 3.6(d). Because of this detrimental ion beam damage, and the lack of perfectly symmetric edge notches, a modified slotted shear specimen was developed inspired by the ASTM B831 standard. A FE model of the specimen geometry is shown in Figure 3.7(a,b), where the slots are terminated with eccentric half-circles that eliminated the stress singularity at the edges of the tip of the notches to achieve near uniform shear stress and shear dominated deformation along and around a zone in the middle of the fiber, as shown in Figure 3.7(c). The FE mesh consisted of 8-node linear brick elements away from the shear zone, and 10-node quadratic tetrahedron elements with increasing mesh density around the shear zone.

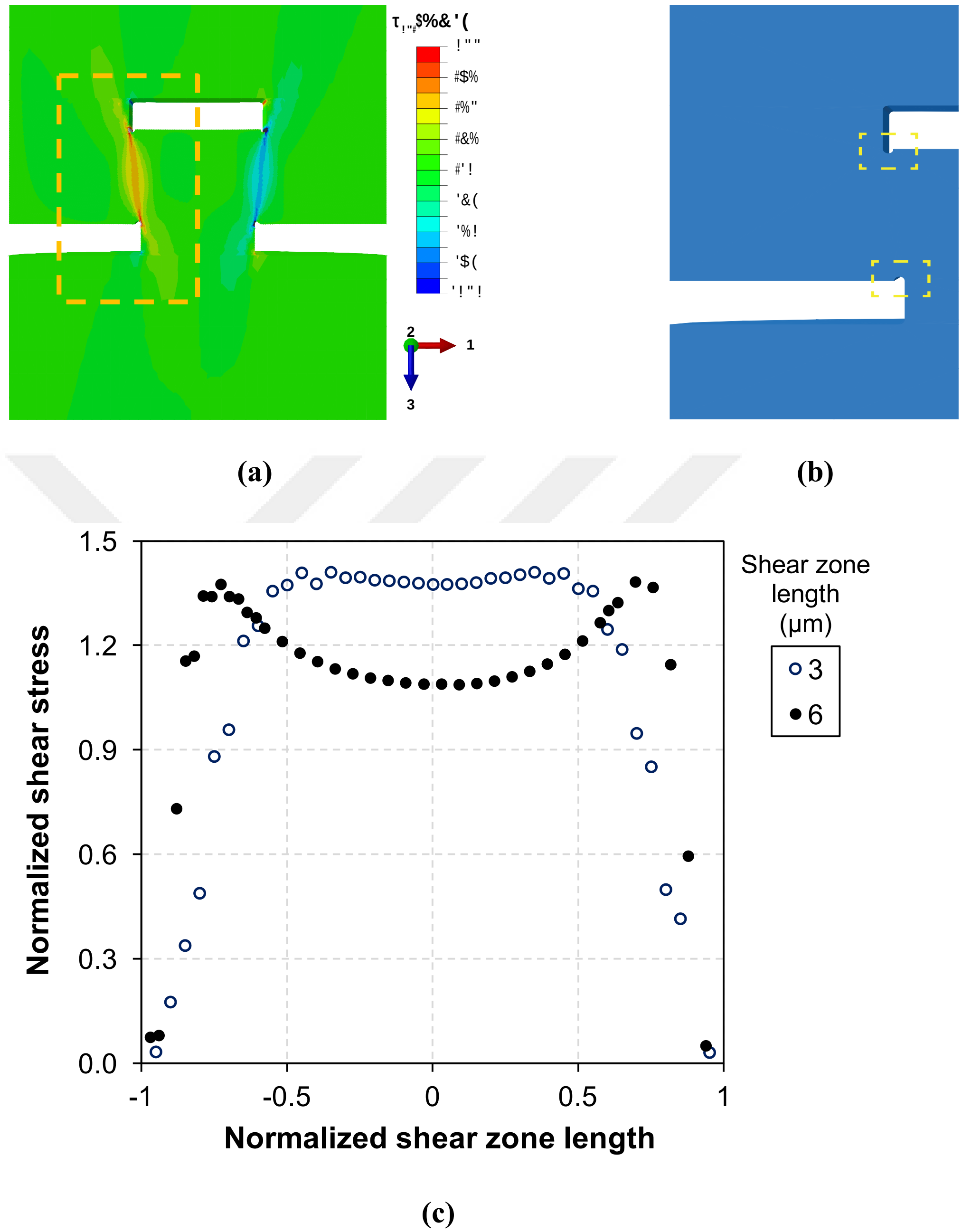

Figure 3.5 (a) FE model of a symmetric double edge-notched specimen with a shear zone length of 3 μm. **(b)** Detail in the area marked in (a), showing the semicircles at the notch tip edges, which were introduced to eliminate the stress singularity. **(c)** Plot of shear stress distribution, demonstrating nearly uniform shear stress along the shear zone, when a 3-μm shear zone length is used.

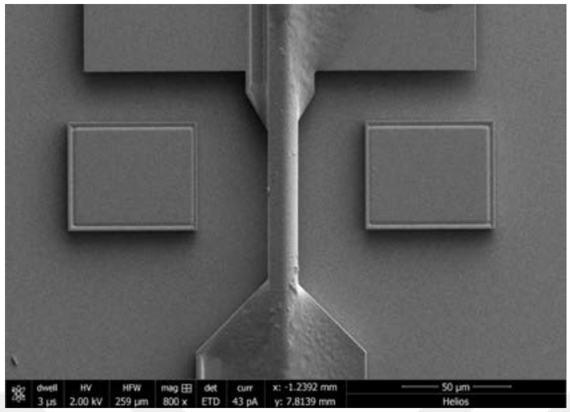

(a)

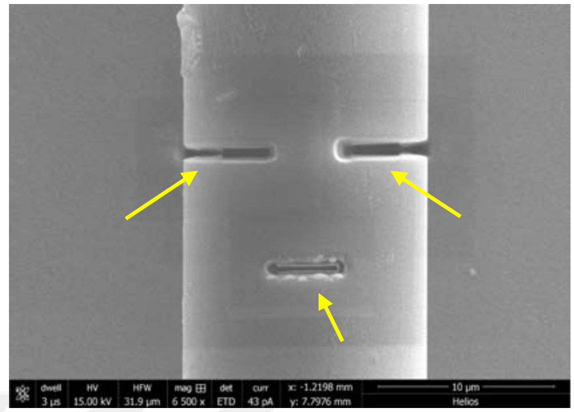

(b)

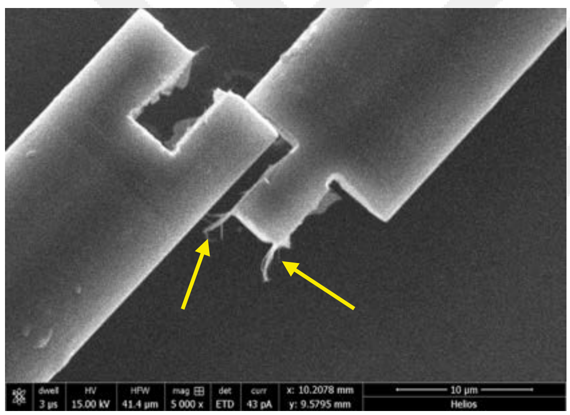

(c)

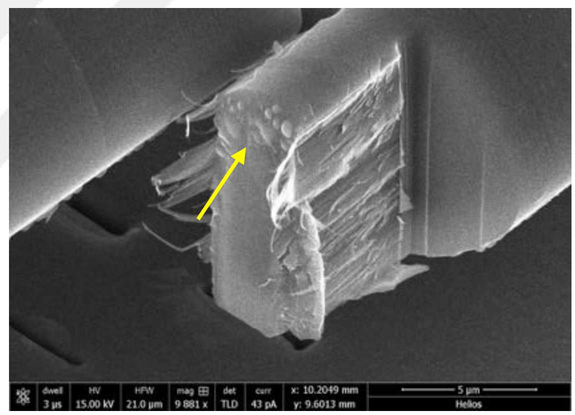

(d)

Figure 3.6 (a) A K49 fiber attached to a MEMS device for microscale fiber testing. **(b)** Notches introduced via a FIB. **(c)** SEM image of matching specimen surfaces after shear failure with the arrows pointing to pulled fibrils. **(d)** FIB damage inside the central slit wall.

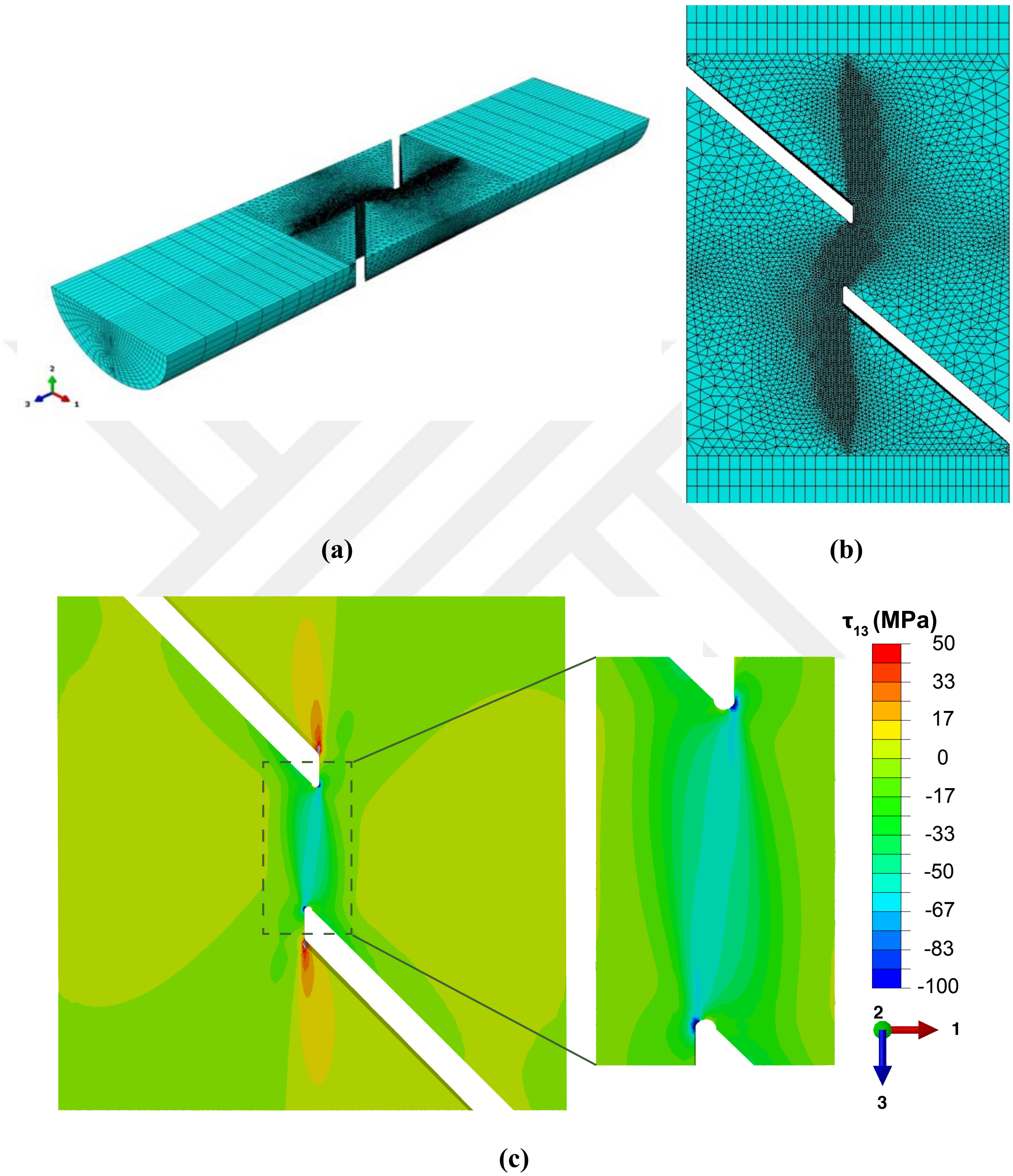

Figure 3.7 (a) FE model of slotted shear specimen, and **(b)** detail of the mesh in the shear zone showing the eccentric semicircles that eliminated the stress singularity at the edges of the shear plane. **(c)** Contour plot of the shear stress demonstrating a near uniform shear dominated deformation along and around the shear zone.

Table 3.2 summarizes the elastic constants used for the transversely isotropic FEA K119 fiber model following the work by Singletary et al. [59]. The elastic modulus values along the fiber axis, E_3, were measured and reported in Chapter 2. The rest of the elastic properties correspond to K29 fibers and are assumed to be similar for other Kevlar fiber grades. The main difference between the fibers is the orientation distribution of crystallites along the fiber axis as shown in Chapter 2, which mainly affects the elastic modulus, E_3, due to the highly anisotropic nature of the monoclinic crystals making up the fibers. Based on this background it is reasonable to assume comparable transverse elastic properties for all Kevlar grades.

Table 3.2. Elastic constants used in the transversely isotropic FEA K119 fiber model following Singletary et al. [59]. The value for E_3 was obtained in the experiments reported in Chapter 2.

E_1, E_2 (GPa)	E_3 (GPa)	G_{13}, G_{23} (GPa)	ν_{12}	ν_{31}
2.45	66	2.2	0.43	0.63

Figure 3.8(a) shows the normalized shear stress, τ_{norm}, on the shear surface of a K119 fiber with 3 μm shear zone length and 0.1 μm radius semicircles at the notch tip edges, Figure 3.8(b). The normalized shear stress is the ratio of the local shear stress, as computed via FEA, to the average shear stress:

$$\tau_{norm} = \frac{\tau}{\frac{F}{A}} \tag{3.1}$$

where F is the applied tensile force on the fiber and A is the area of the shear plane. The Ga^+ ions of the FIB could amorphize the polymer in the vicinity of the notch tip edges. By shaping the stress profile to result in a non-singular stress state at the notch tip, the shear stress vanishes in the potentially amorphized regions, thus preventing premature

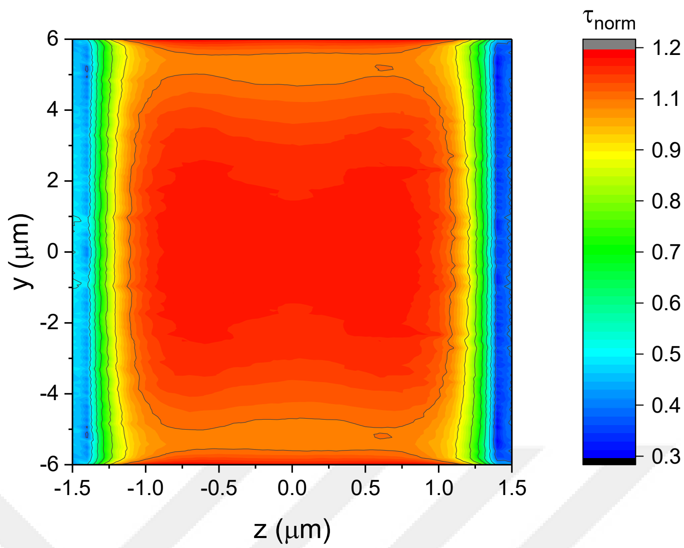

(a)

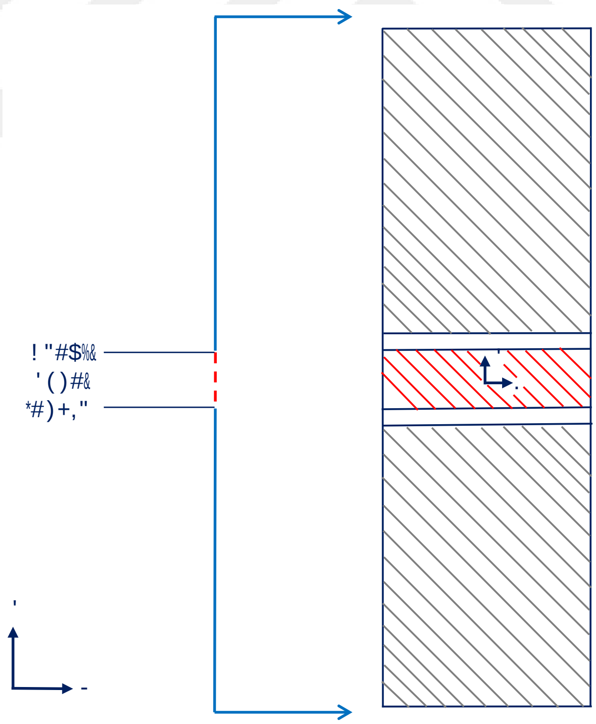

(b)

Figure 3.8 (a) Normalized shear stress on the shear zone surface. **(b)** Fiber with 3-μm shear zone length and 0.1 μm radius semicircles at the notch tip edges, showing the origin at the center of the shear zone.

failure due to FIB-induced damage. Moreover, as deduced from Figure 3.8(a), the shear stress profile is uniform in the majority of the shear surface in the central region of the fiber while the highest shear stress occurs along the central line (x = 0, y = 0). Thus, the specimen geometry could be optimized based on a comparison of shear stress profiles along the central line in the shear zone. This is demonstrated in Figure 3.9 where the normalized shear stress is plotted along the central line for various shear zone length values. In the plot, the normalized coordinates 1 and -1 correspond to the notch tip. It is observed that a shear zone length of 3 μm could provide a nearly uniform shear stress profile for at least half of the shear zone length. The shear strength can be directly computed from the peak force at failure by dividing with the shear zone area, and multiplying by the factor 1.16 which corresponds to the plateau for the case of 3 μm in Figure 3.9. The stress distribution shown in Figure 3.8(a) guarantees that shear failure will occur when the peak stress along the central line reaches the shear strength of the material.

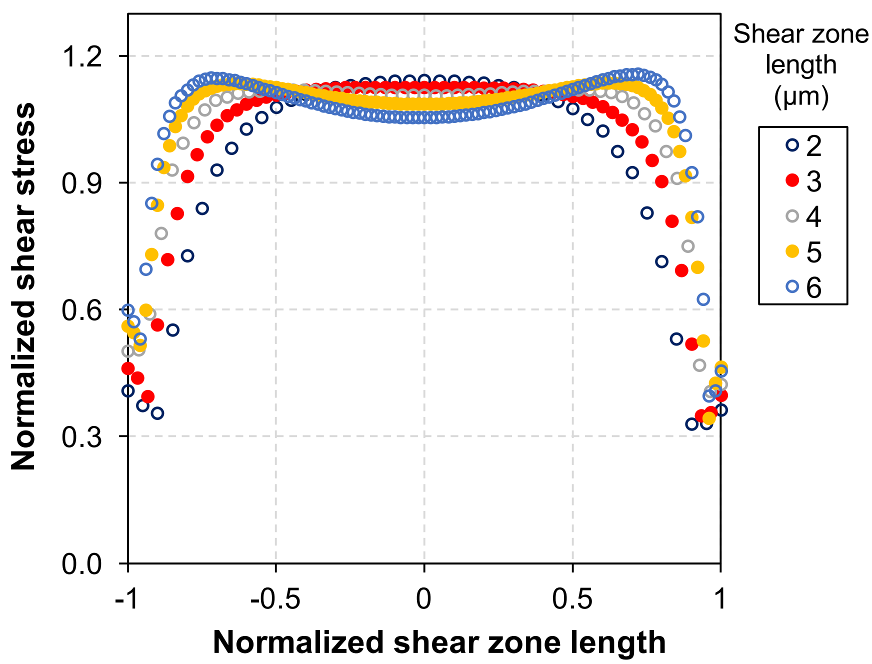

Figure 3.9 Shear stress profiles along the central line, (x = 0, y = 0) in Figure 3.8(b), for a K119 fiber with different shear zone lengths.

The pulled fibrils observed in the shear zone in Figure 3.6 may also be due to the influence of the non-zero tensile stress component in the shear zone. Similarly, the value of the normal stress in the transverse direction, σ_{11}, which could result in opening of a crack in the transverse direction may also affect the calculated shear strength. To assess the potentially important role of σ_{11} and σ_{33} in the measured tensile force value that drives shear failure, their values in the shear zone are plotted in Figure 3.14(a,b), respectively. For van der Waals interactions, that hold the fiber structure together in the transverse direction, 100 MPa is a reasonable cohesive strength value which is much larger than the spectrum of values in the contour plot in Figure 3.14(a). Similarly, the values of σ_{33} in Figure 3.14(b) are more than two orders of magnitude smaller than the 4 GPa tensile strength of K119 fibers, and several times smaller than the reported compressive strength of aramid fibers of 300-700 MPa [56,121]. Therefore, the tensile components of stress in the shear zone are not expected to cause tensile fibril failure or microbuckling.

In summary, the asymmetric shear specimen geometry exhibits shear stress profiles that ensure accurate shear strength measurements in high performance micrometer scale fibers. Yet, during specimen preparation, the notch geometry cannot be precisely defined due to limitations in nanoscale milling via FIB [122]. The angle of the notch, 45°, does not deviate by an appreciable amount. However, the intended 3 μm shear zone length could be defined within the 2.5-3.5 μm range. According to the plot in Figure 3.9 this range in shear zone length results in τ_{norm} in the range 1.13-1.18, while still maintaining the plateau in the middle of the shear zone, whose length can be measured quite precisely before testing using SEM. Finally, the role of the variation of the semicircle radius through the fiber thickness was evaluated via a FEA for a 3-μm zone length and different semicircle radii. Figure 3.11 shows that the maximum τ_{norm} along the center line varies in the range 1.16-1.2 suggesting a minimal effect on the calculated shear strength. While a 0.05 μm radius is very small for ion-mill using a FIB, 0.1-0.2 μm radii could be machined properly and showed nearly uniform shear stress profile. Therefore a 0.1 μm radius was used in the calculations shown in Figure 3.9.

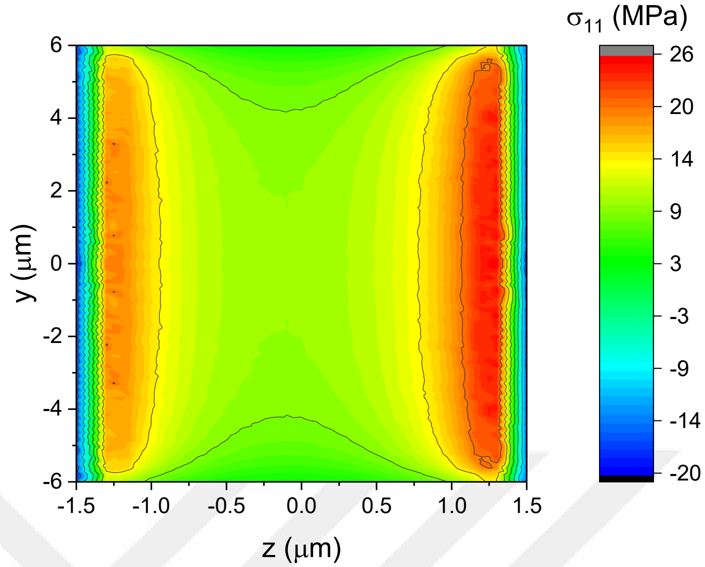

(a)

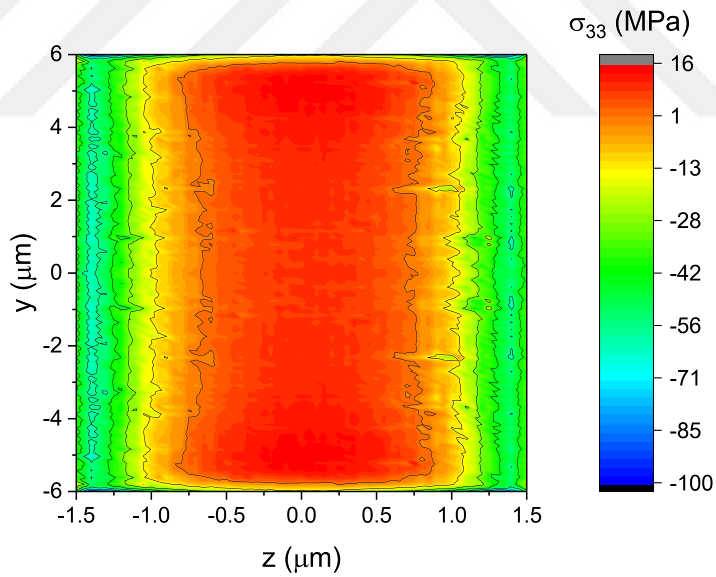

(b)

Figure 3.10 (a) Normal stress in transverse direction, σ_{11} and **(b)** tensile stress σ_{33} in the shear zone at the point of shear failure.

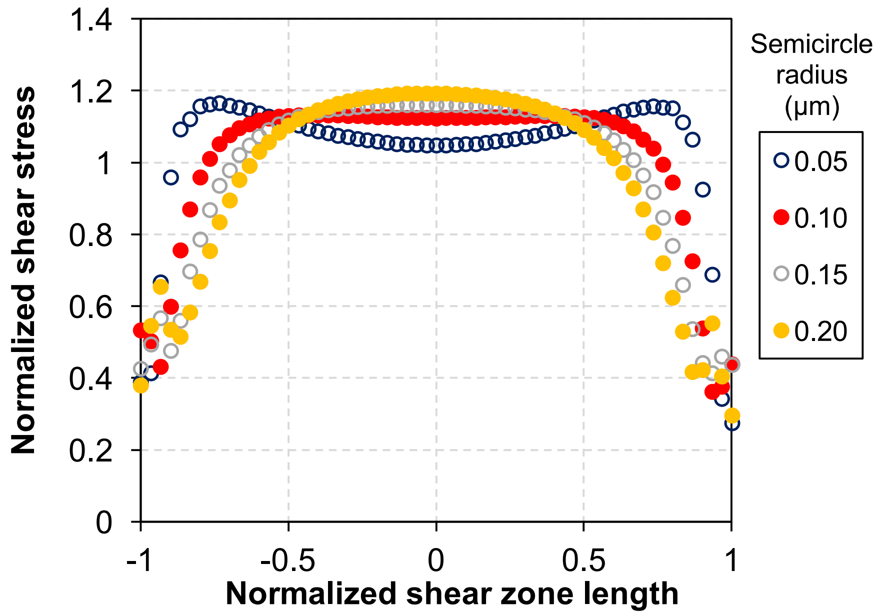

Figure 3.11 Shear stress profiles along the central line, (x = 0, y = 0) in Figure 3.8(b), for a K119 fiber with 3-µm shear zone length and different semicircle radii.

The two edge notches could be off-axis by a distance, δ, that could be as much as 0.5 µm, as described in the schematic in Figure 3.12(a). This issue could arise due to the non-circular fiber cross-section and tilt in sample during FIB milling. A FE analysis was performed for a fiber with 3 µm shear zone length, 0.1 µm semicircle radius and various out-of-axis values. As shown in Figure 3.12(a), the off-axis distance did not affect the value of τ_{norm}. For two edge notches with non-zero off-axis distance, the shear surface area could be calculated quite precisely by using SEM images. Finally, the eccentricity of the two notches was considered as described in the schematic in Figure 3.12(b). SEM observations pointed out that FIB-generated edge notches could be eccentric by as much as e = 0.25 µm. A FE analysis of a fiber with 3 µm shear zone length, 0.1 µm semicircle radius showed that eccentricity is the most important factor to be considered during FIB milling, as the typical eccentricity of 0.25 µm results in ~10% difference in the calculated shear strength compared to a perfect specimen. It should be noted that this difference could be accounted for by measuring the eccentricity with SEM before testing and using the corresponding τ_{norm} value from the plots.

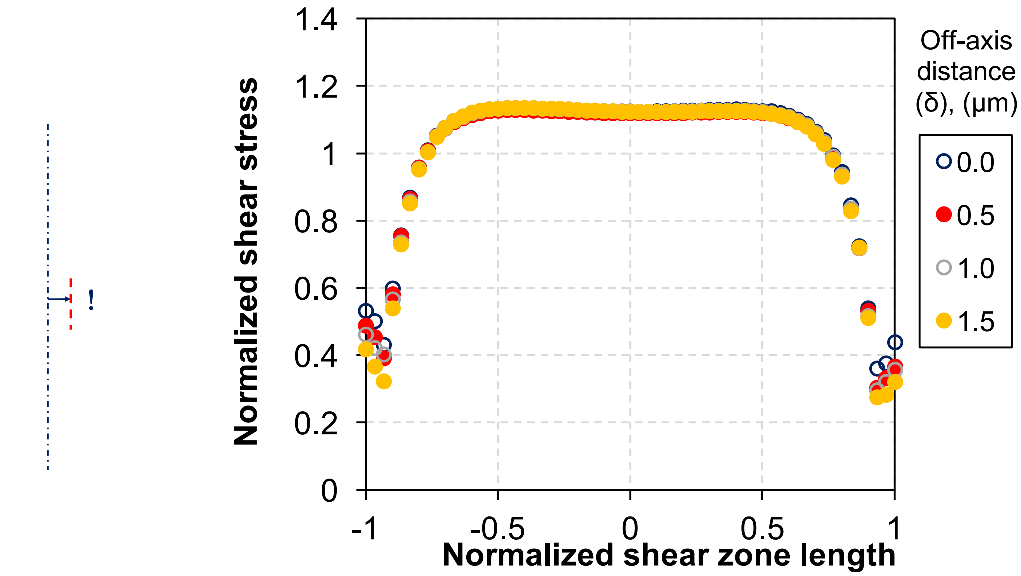

(a)

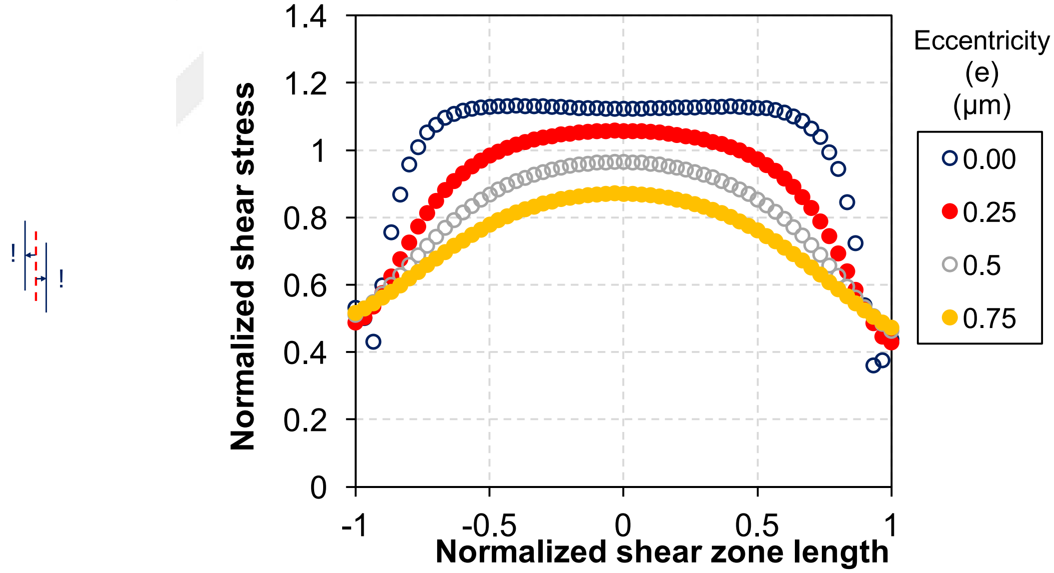

(b)

Figure 3.12 (a) Schematic of a fiber in which the shear surface is off-axis, and corresponding plot of the normalized shear stress in the shear zone. Note that the actual shear surface area was used for shear stress normalization. **(b)** Schematic of a fiber with eccentric edge notches and plot of normalized shear stress in the shear zone showing that a typical eccentricity of 0.25 μm results in 10% uncertainty in the measured shear strength. This issue can be addressed by measuring the eccentricity before testing.

3.2.2 *Shear Strength Measurements*

Figure 3.13(a) shows the MEMS device custom designed at UIUC for the shear tests and fabricated by using the PolyMUMPS process of MEMSCAP (NC, USA). Movable structure of the device was built up of two stacked polycrystalline silicon layers (POLY1 and POLY2 layers of PolyMUMPS process) with total thickness of 3.5 μm so as to achieve high out-of-plane bending stiffness. The thicker device allowed us to position a fiber inside a channel that was fabricated directly by photolithography. While placed in this channel, a fiber sits closer to the neutral axis of the MEMS device, hence reducing the out-of-plane bending moment under a tensile force [90]. The device design consists of a pedal where a glass probe is attached to extend the fiber with the aid of an external piezoelectric actuator. External actuation overcomes several and significant inherent issues in on-chip MEMS actuation, and allows for generating forces of the order of mN, which is not easy to do with on-chip actuators. By DIC of high magnification optical microscopy images, the rigid body motion of the numbered pads in Figure 3.13(b) was calculated with ~20 nm resolution [123]. This MEMS device enables the simultaneous measurement of the force applied on the fiber by an external actuator [124] as the product of loadcell stiffness × ($u_{II} - u_{III}$), and the fiber elongation as (u_I-u_{II}), where u_I, u_{II} and u_{III} are the rigid body displacements of the three numbered pads in Figure 3.13(b). The as-fabricated, folded beam type, loadcell was designed to have a maximum stiffness of 2400 N/m; smaller stiffness values are achieved by cutting a number of the parallel beams using a FIB, in order to increase the sensitivity of the loadcell for a given stiffness of the test fibers.

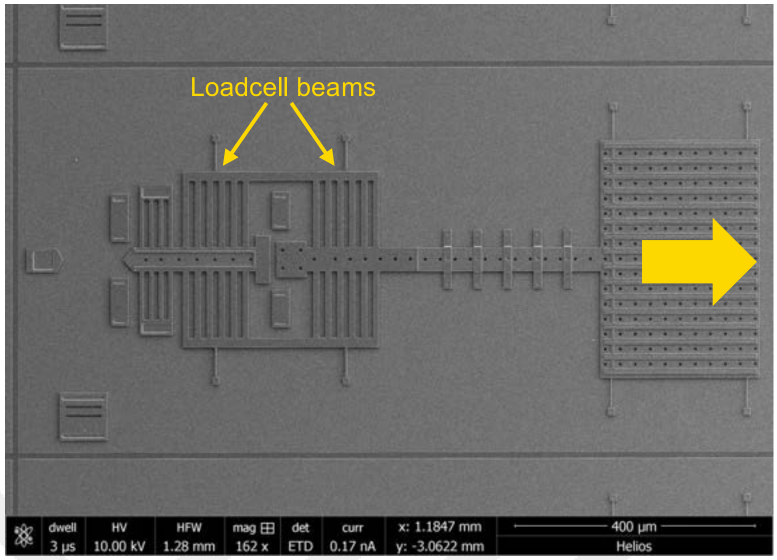

(a)

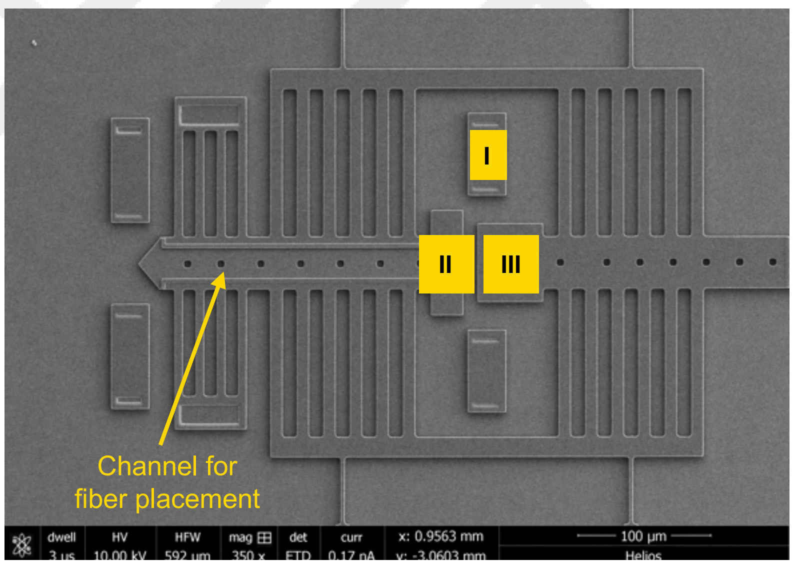

(b)

Figure 3.13 (a) MEMS tensile tester with a folded beam type loadcell. The arrow on the pedal points to the direction of actuation with the aid of an external piezoelectric actuator. **(b)** Close-up of the device loadcell and grip: A fiber is placed inside the channel while the rigid body motion of the three numbered pads simultaneously provides measurements of the applied force and the fiber stretch ratio or engineering strain.

3.3 Results and Discussion

Figure 3.14(a) shows a notched K119 fiber attached to a MEMS device, with the details of the notched test specimen shown in Figure 3.14(b,c). As shown in the figures, the ion beam used to shape the test fiber has caused minimal damage compared to the symmetric double shear specimen shown in Figure 3.6(b) due to the reduced time of exposure to the ion beam. For the particular edge notches, the milling current was 2 nA at 16 kV voltage.

Figure 3.15 shows a plot of the maximum shear stress vs. cross-head displacement for a K119 fiber which, at the peak tensile force, failed along the uniform stress portion of the shear zone shown in Figure 3.8(b). The non-linearity of the curve is due to the deformation of the compliant epoxy used to attach the fiber to the MEMS device. The true shear strength was 81 MPa. The average shear strength of 85±7.6 MPa was calculated for three K119 fibers by carefully measuring the shear zone length, semicircle radius, off-axis distance and eccentricity of the FIB milled specimens before testing and using the τ_{norm} calculated using the FE analysis for the specific geometric parameters, as summarized in Section 3.2.1. Past work on shear strength measurements of aramid filaments utilized tension testing of untwisted single fibers previously twisted to increasing torsional strain and measuring the torsional strain at the point that the fiber tensile strength decreased [56,61,85]. The shear strength was calculated from the torsional strain by assuming that the maximum shear stress develops on the periphery of the fiber where the skin-core interface resides. The shear strength, $\tau_{\theta z}$, values of various experimental and commercial aramid filaments were reported to be in the range of 25-180 MPa. This large variation of shear strength values measured using torsional tests may also be, in part, due to the skin-core interface which, as shown in Chapter 2, can be weak. Hence, these values of shear strength are not a correct measure of the interfibrillar shear interactions. The shear strength measured in this dissertation research study utilized a uniform shear test, thus could capture the interfibrillar shear interactions with minimal influence of the weak skin-core interface that is a limiting factor for the tensile strength of aramid fibers.

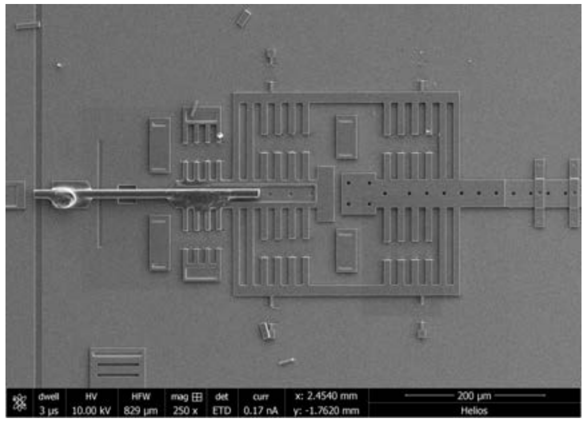

(a)

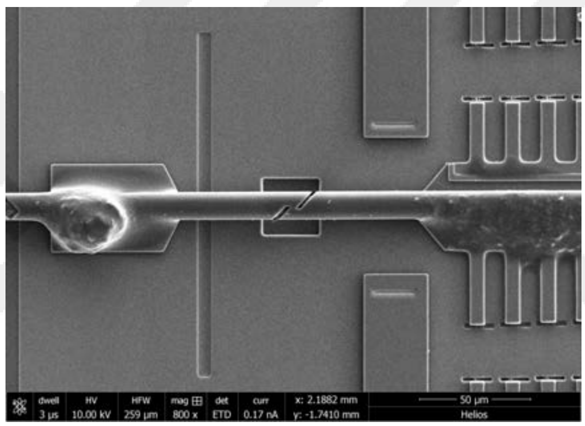

(b)

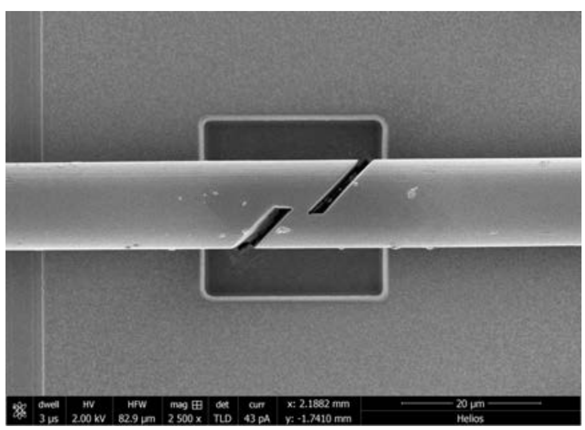

(c)

Figure 3.14 (a) A K119 fiber placed onto a MEMS device. **(b)** Fiber after the edge notches were created via a FIB. **(c)** Close-up view showing minimal damage on the fiber surface.

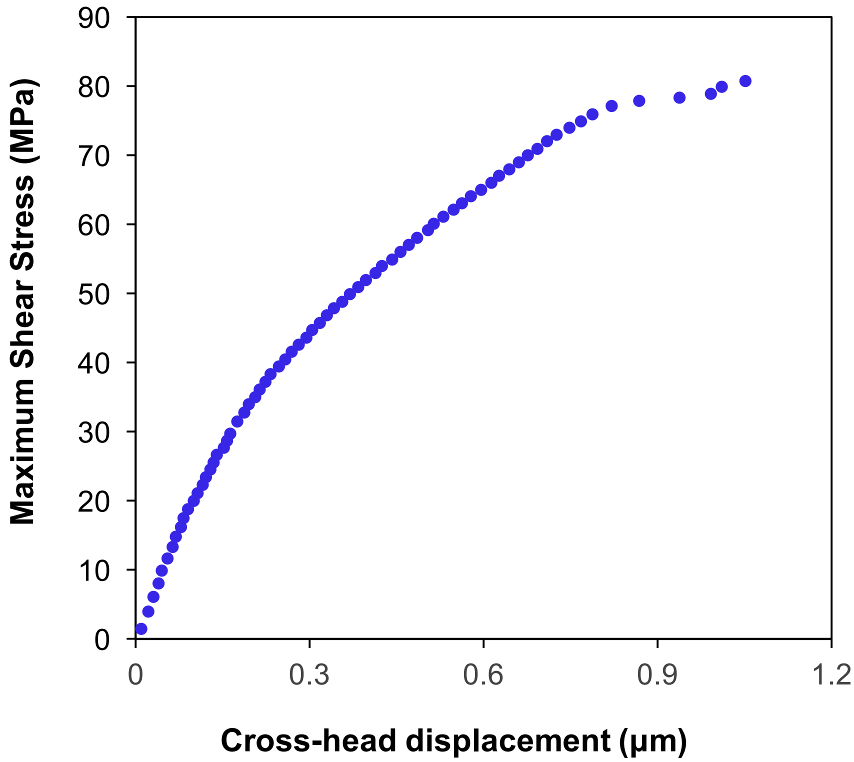

Figure 3.15 Shear stress vs. cross-head displacement of a K119 fiber with true shear strength of 81 MPa.

The present shear tests also revealed the internal structure of the K119 fibers. Figure 3.16(a) shows a K119 fiber after shear failure with fine fibrillar structure consisting of multiple size fibrils, Figure 3.16(b,c), which supports the hypothesis presented in Chapter 2 that there is not intrinsic length scale for the fibrils but the loading conditions determine fiber splitting and the spontaneously exposed "internal structure" during fiber failure. Figure 3.16(d) shows multiple sheets of fibrils that were sheared during mode II failure due to the dynamic fracture process that initiated failure in multiple parallel planes. Another important observation of the fracture surfaces was the clear skin-core differentiation and the different structure of the two components of the fiber. Figure 3.17(a) shows a missing skin fragment on one side of a K119 shear specimen, which is found on the matching side of the specimen in Figure 3.17(b). Skin fragments consistently peeled off from the fiber surface with sizes as long as ~6 μm,

Figure 3.17(c), suggesting a weak skin-core interface. This was also pointed out as the reason for failure initiation in the short gauge length fibers (200 μm) discussed in Chapter 2. SEM images of the inner surface of a skin fragment, Figure 3.17(d), showed no fibrillar structure as opposed to the fibrillar core.

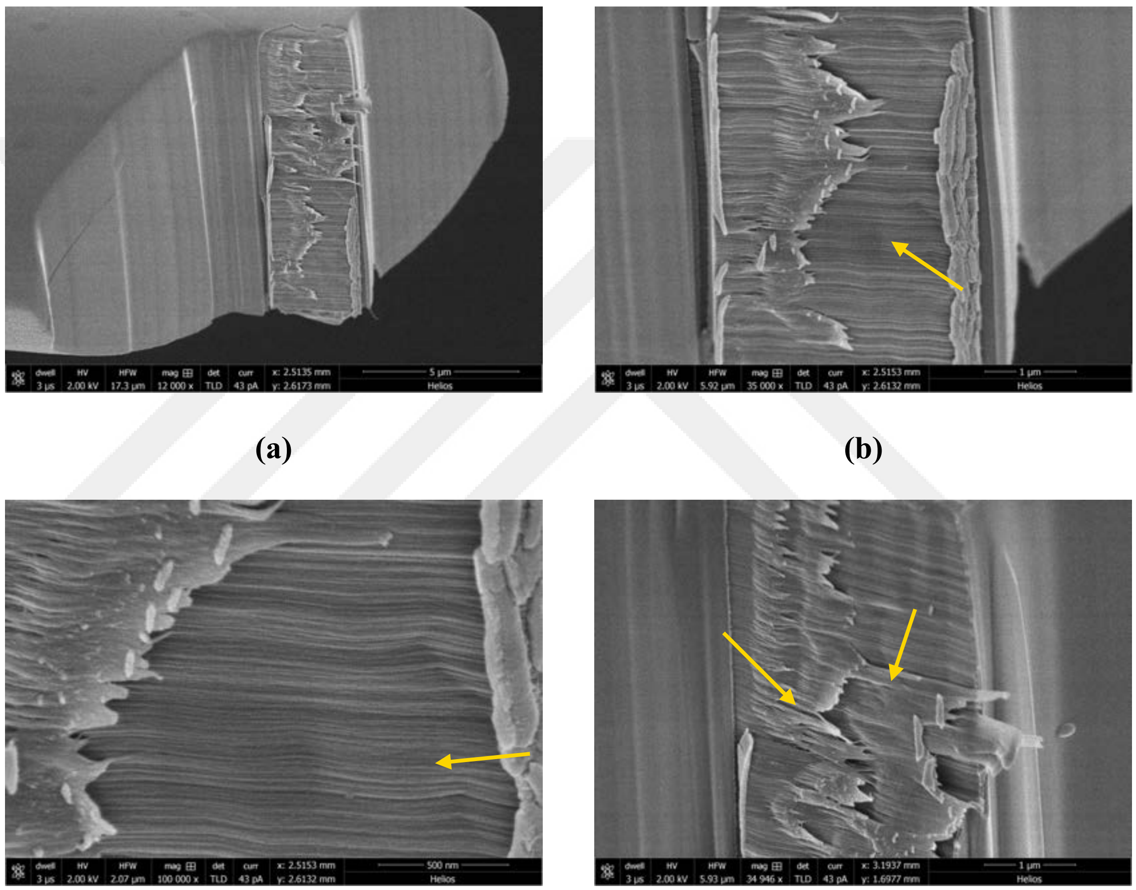

(a) **(b)** **(c)** **(d)**

Figure 3.16 (a) SEM image of a K119 fiber after shear failure. **(b,c)** fine fibrillar structure. **(d)** Parallel sheets of split fibrils indicating shear failure.

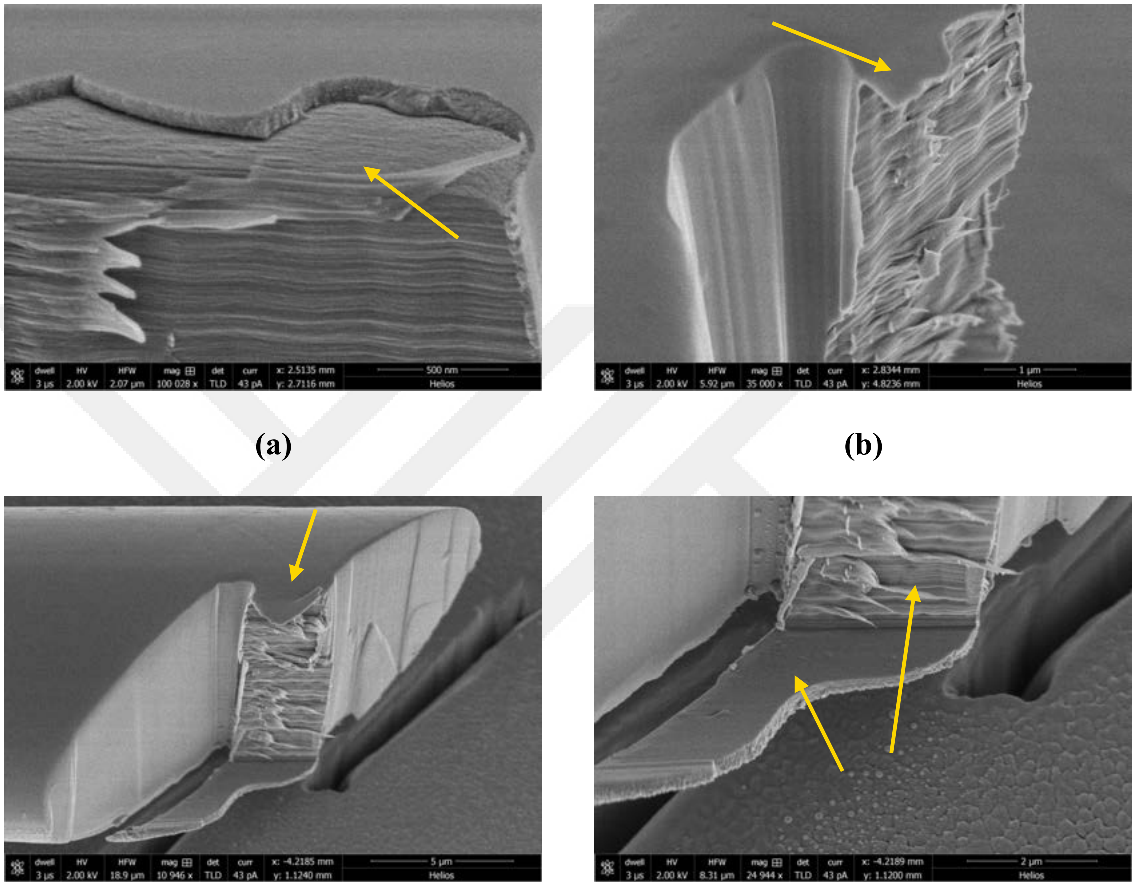

(a) (b) (c) (d)

Figure 3.17. (a) Skin fragment missing on one side of a K119 shear specimen, and **(b)** matching side containing the particular skin fragment. **(c,d)** Skin fragments as long as ~6 μm with distinct non-fibrillar structure compared to fibrillar structure of the fiber core.

3.4 Conclusions

The first of the kind uniform shear experiments with high performance aramid fibers using a custom designed MEMS device were performed. Careful design of the shear test specimen via a FE analysis resulted in a uniform shear stress profile along a shear zone in the fiber specimen. The specimen design eliminated the stress singularity at the notch tip and ensured that the uniform shear stress in the majority of the shear zone was also the highest shear stress in the test specimen. Using this experimental approach, the average shear strength of K119 fibers was calculated as 85±7.6 MPa. The failure surfaces were characterized by a fine fibrillar structure comprised of parallel sheets of split fibrils, which is similar to the multiple axial splits forming under uniaxial tension, thus suggesting shear driven failure even under tensile loading. The weak interface between the fiber skin and the core was manifested as skin debonding around the shear zone.

CHAPTER 4

CONCLUSIONS

This dissertation research aimed at understanding the effect of micro-and nano-structure on the tensile behavior and tensile strength of high performance aramid fibers. Towards this goal, high quality commercial aramid fibers, Kevlar®, with different orientation distributions were studied under different loading conditions to probe the effect of crystalline domain orientation on the mechanical properties.

XRD measurements were performed on bundles of fibers to quantify the orientation distribution and FWHM, which is a measure of the misorientation of crystalline domains comprising the fiber microstructure. Three different types of as-spun and one type of heat-treated fibers were employed in this study with initial distributions of crystallite orientation between 16.7º and 9.7º with respect to the fiber axis. The tensile response of single aramid filaments was nonlinear for the largest values of FWHM, with a clear transition regime at ~2% strain leading to higher stiffness. This transition regime gradually disappeared with increasing fiber orientation such that the stress-strain behavior morphed into a bilinear curve for the highest orientation fibers or fibers that were mechanically conditioned to reach higher crystalline domain orientation. The values of the Young's modulus of the initially linear regime correlated perfectly with the FWHM, and independently of the applied strain rate, varied in a limited range, supporting a linear elastic behavior at strain values below 0.5%.

The different regimes of deformation during monotonic loading were due to the evolution of crystalline domain orientation. The latter was investigated via loading-unloading tests to increasing peak stress, similar to mechanical conditioning. This process increased both the initial and the final fiber modulus and linearized the stress-strain curve, an effect that was retained upon unloading, and was attributed to increased crystalline domain orientation in the fibers. Importantly, this re-orientation process was shown to be independent of the loading path.

The initial distributions of crystallite orientation between 16.7º and 9.7º, corresponded to initial moduli between 66 GPa and 119 GPa, and tensile strength values in the range of 3.5-4.0 GPa. Cyclic loading up to 90% of the tensile strength of each filament type increased the initial and final moduli of non-heat treated fibers: the initial modulus of all fiber types converged to 100 GPa, corresponding to a stable crystallite orientation distribution of 11.6º, while the initial unloading modulus converged to ~165 GPa, close to the theoretical modulus of 220 GPa, corresponding to an orientation distribution of 5.8º, which, however, was not retained upon unloading. The loading modulus of oriented as-spun fibers was quite smaller than the modulus of 120 GPa of aramid fibers subjected to post-spin heat treatment, for which, mechanical cycling affected only the initial unloading modulus which, after cycling to 90% of the average tensile strength, converged to 170 GPa. Tests done at different strain rates that were more than three orders of magnitude apart showed that the permanent orientation of crystalline domains at high strains/stresses scales inversely with the applied strain rate: The increase in permanent orientation of crystalline domains is possible by sliding of crystallites through rate dependent breaking of intercrystal van der Waals bonds and reforming in new energetically favorable positions. Most notably, at strain rates of 0.2-0.3 s^{-1} both as-spun and heat-treated fibers were linearly elastic until failure.

In all cases, although mechanical cycling could increase the initial modulus by as much as 54%, the tensile strength remained constant before and after conditioning. It is, thus, deduced that the tensile strength may be controlled by either preexisting defects or other aspects of the fiber microstructure. Experiments showed constant tensile strength for gauge lengths as short as 200 μm, thus, implying that failure is not due to flaws obeying the weakest link statistics. Instead, short gauge length tests (200 μm) of all fiber types showed failure initiation near the skin-core interface, which allowed the extrusion of the fiber core. Thus, the microstructural differentiation between the fiber core and the skin is the likely limiting factor in tensile strength of aramid fibers.

The crystallite orientation process during mechanical loading requires significant local shear deformation, which, based on a relatively common FWHM limit value (5.8º) attained by all fibers types after loading to 90% of tensile strength, was hypothesized to be a controlling factor in fiber failure. To this effect, quantitative shear tests were performed for the first time using individual aramid fibers with edge notches whose shape, dimensions and spacing were optimized through a FEA and created by a FIB, to ensure shear dominant deformation and failure in the region of interest. The fragile nature of the test specimens required custom designed MEMS devices for small scale testing. By this method the shear strength for K119 was found to be 85±7.6 MPa. Post-mortem SEM images of the shear failure surfaces revealed a fine fibrillar structure and multiple sheets of fibrils which are reminiscent of the multiple axial splits typically observed in fibers tested in tension. SEM images of shear failure surfaces also pointed out to a skin-core differentiation and a weak interface which resulted in fragments of skin that debonded around the shear zone.

4.1 Future Prospects

The studies pursued in this dissertation research revealed several challenges and opportunities for future research, which are briefly discussed in this Section.

4.1.1 Improved in situ XRD Studies with Mechanical Loading

The XRD system that was available for this research at the Materials Research Laboratory presented us with two limitations. First, although mechanical testing was performed with individual fibers, all XRD measurements were performed on bundles containing hundreds of fibers. Future studies could utilize synchrotron radiation sources to study the crystallite orientation at the single fiber scale with higher accuracy than bundle measurements, and the ability to investigate the differentiation between the fiber skin and the core by utilizing recent micro-beam diffraction advances. The second limitation was the lack of a capability to obtain XRD scans during loading. Although the crystallite orientations corresponding to the initial reloading and initial unloading moduli of mechanically conditioned fibers were inferred using an analytical model, in situ mechanical loading under a diffractometer would open new possibilities in obtaining further understanding of the mechanics of aramid fibers.

4.1.2 In Situ Mechanical Testing of Single Aramid Fibers under an AFM

Post mortem SEM images of tested fibers elucidated the importance of skin-core differentiation in aramid fibers. The fiber skin did not have the fine fibrillar structure of the core, while the split skin-core interfaces evidenced in SEM images raised the hypothesis of skin failure as the limiting factor in tensile strength. Preliminary *in situ* SEM imaging did not show any damage of the K119 fiber surface up to ~75% of the failure strain, Figure 4.1(a). On the other hand, the electron beam sensitivity of aramid fibers severely limited higher magnification imaging to reveal the finer details, resulting in cracks on the fiber surface, Figure 4.1(b), due to breaking of bonds under the combined effect of mechanical loading and electron beam irradiation [125]. *In situ* tension testing under an AFM not only would prevent deterioration of the fiber structure, but also enable the detection of possible nanometer scale damage and fibrillation of the skin, which could shed further light into the effect of skin-core differentiation on the tensile strength of aramid fibers.

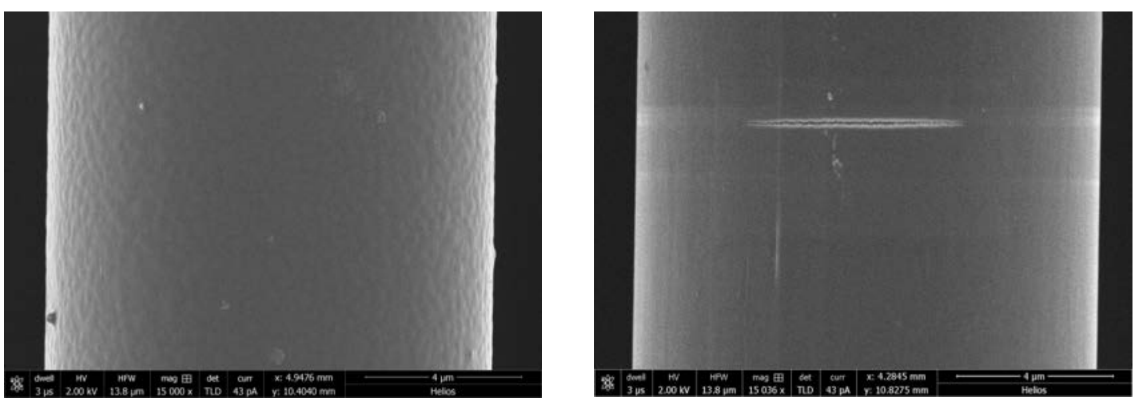

(a) **(b)**

Figure 4.1 (a) K119 fiber loaded *in situ* inside an SEM to ~75% of failure strain without showing damage on the outer fiber surface. **(b)** Higher magnification imaging resulted in cracks on the fiber surface due electron beam damage combined with tensile loading.

REFERENCES

[1] H. H. Yang, *Kevlar aramid fiber*. John Wiley & Sons Ltd., 1993.

[2] K. K. Chawla, *Composite Materials: Science and Engineering*. Springer - Verlag, 2012.

[3] du Pont de Nemours, “Kevlar Aramid Fiber Technical Guide,” 2000.

[4] D. Ahmed, Z. Hongpeng, K. Haijuan, L. Jing, M. Yu, and Y. Muhuo, “Microstructural Developments of Poly (p-phenylene terephthalamide) Fibers During Heat Treatment Process: A Review,” *Materials Research*, vol. 17, no. 5, pp. 1180–1200, Jan. 2014.

[5] H. G. Chae and S. Kumar, “Rigid-Rod Polymeric Fibers,” *Journal of Applied Polymer Science*, vol. 100, no. 1, pp. 791–802, 2006.

[6] L. Penn, H. A. Newey, and T. T. Chiao, “Chemical characterization of a high-performance organic fiber,” *Journal of Materials Science*, vol. 11, no. 1, pp. 190–191, 1976.

[7] P. J. Burchill, “Chemical characterization of Kevlar-49,” *Journal of Materials Science*, vol. 13, no. 10, pp. 2275–2276, 1978.

[8] S. J. Picken, D. J. Sikkema, H. Boerstoel, T. J. Dingemans, and S. van der Zwaag, “Liquid crystal main-chain polymers for high-performance fibre applications,” *Liquid Crystals*, vol. 38, no. 11, pp. 1591–1605, 2011.

[9] M. Grujicic, P. S. Glomski, B. Pandurangan, W. C. Bell, C. F. Yen, and B. A. Cheeseman, “Multi-length scale computational derivation of Kevlar® yarn-level material model,” *Journal of Materials Science*, vol. 46, no. 14, pp. 4787–4802, 2011.

[10] M. G. Northolt and J. J. van Aartsen, “On the Crystal and Molecular Structure of Poly-(P-Phenylene Terephthalamide),” *Journal of Polymer Science: Polymer Letters Edition*, vol. 11, no. 5, pp. 333–337, May 1973.

[11] M. G. Northolt, “X-Ray-Diffraction Study of Poly(P-Phenylene Terephthalamide) Fibers,” *European Polymer Journal*, vol. 10, no. 9, pp. 799–804, 1974.

[12] M. G. Northolt and J. J. van Aartsen, “Chain Orientation Distribution and Elastic Properties of Poly (p-phenylene terephthalamide), A ‘Rigid Rod’ Polymer,” *Journal of Polymer Science: Polymer Symposium*, no. 58, pp. 283–296, 1977.

[13] K. Tashiro, M. Kobayashi, and H. Tadokoro, “Elastic-Moduli and Molecular-Structures of Several Crystalline Polymers, Including Aromatic Polyamides,” *Macromolecules*, vol. 10, no. 2, pp. 413–420, 1977.

[14] S. L. Kwoleck, “Wholly aromatic carbocyclic polycarbonamide fiber having orientation angle of less than about 45 degrees,” 3,819,587, 1974.

[15] R. J. Morgan, C. O. Pruneda, and W. J. Steele, “The Relationship Between the Physical Structure and the Microscopic Deformation and Failure Processes of Poly(P-Phenylene Terephthalamide) Fibers,” *Journal of Polymer Science: Polymer Physics Edition*, vol. 21, no. 9, pp. 1757–1783, 1983.

[16] Y. Onogi, J. L. White, and J. F. Fellers, “Structural Investigations of Polymer Liquid-Crystalline Solutions: Aromatic Polyamides, Hydroxy Propyl

Cellulose, and Poly(Gamma-Benzyl-L-Glutamate)," *Journal of Polymer Science: Polymer Physics Edition*, vol. 18, no. 4, pp. 663–682, 1980.

[17] S. J. Picken, S. van der Zwaag, and M. G. Northolt, "Molecular and macroscopic orientational order in aramid solutions: a model to explain the influence of some spinning parameters on the modulus of aramid yarns," *Polymer*, vol. 33, no. 14, pp. 2998–3006, 1992.

[18] G. C. Rutledge, U. W. Suter, and C. D. Papaspyrides, "Analysis of Structure of Polymorphism in Poly (p-phenyleneterephthalamide) through Correlation of Simulation and Experiment," *Macromolecules*, vol. 24, no. 8, pp. 1934–1943, 1991.

[19] H. S. Morgan, "Process for Spinning Wholly Aromatic Polyamide Fibers," 3,414,645, 1968.

[20] H. Blades, "Dry jet wet spinning process," 3,767,756, 1973.

[21] K. G. Lee, R. Barton, and J. M. Schultz, "Structure and Property Development in Poly(P-Phenylene Terephthalamide) During Heat Treatment Under Tension," *Journal of Polymer Science: Polymer Physics Edition*, vol. 33, no. 1, pp. 1–14, 1995.

[22] R. J. Morgan and R. E. Allred, "Aramid Fiber Reinforcements ," in *Reference Book for Composites Technology v.1*, S. M. Lee, Ed. Technomic Publishing Company, Inc., 1989, pp. 143–166.

[23] E. E. Magat, "Fibres from extended chain aromatic polyamides," *Philosophical Transactions of the Royal Society of London A: Mathematical, Physical and Engineering Sciences*, vol. 294, no. 1411, pp. 463–472, 1980.

[24] S. Rebouillat, "Aramids," in *High Performance Fibres*, J. W. S. Hearle, Ed. 2001, pp. 23–61.

[25] S. Ran, D. Fang, X. Zong, B. S. Hsiao, B. Chu, and P. M. Cunniff, "Structural changes during deformation of Kevlar fibers via on-line synchrotron SAXS/WAXD techniques," *Polymer*, vol. 42, no. 4, pp. 1601–1612, 2001.

[26] M. G. Dobb, D. J. Johnson, and B. P. Saville, "Direct Observation of Structure in High-Modulus Aromatic Fibers," *Journal of Polymer Science Part C-Polymer Symposium*, no. 58, pp. 237–251, 1977.

[27] B. J. Chu, C. Wu, Y. J. Li, G. S. Harbison, E. J. Roche, S. R. Allen, T. F. McNulty, and J. C. Phillips, "Synchrotron X-Ray-Diffraction of a Single Filament and a Bundle of Poly(P-Phenylene Terephthalamide) Filaments," *Journal of Polymer Science: Polymer Letters Edition*, vol. 28, pp. 227–232, 1990.

[28] R. J. Davies, C. Koenig, M. Burghammer, and C. Riekel, "On-axis microbeam wide-and small-angle scattering experiments of a sectioned poly (p-phenylene terephthalamide) fiber," *Applied Physics Letters*, vol. 92, no. 10, p. 10193, 2008.

[29] A. M. Hindeleh, N. A. Halim, and K. A. Ziq, "Solid-State Morphology and Mechanical Properties of Kevlar 29 Fiber," *Journal of Macromolecular Science, Part B*, vol. 23, no. 3, pp. 289–309, 1984.

[30] L. R. G. Treloar, "Calculations of Elastic Moduli of Polymer Crystals: I. Polyethylene and Nylon 66," *Polymer*, vol. 1, pp. 95–103, 1960.

[31] G. S. Fielding-Russell, “Estimation of the elastic modulus of fully aromatic polyamide fibers,” *Textile Research Journal*, pp. 861–864, 1971.
[32] R. J. Gaymans, J. Tijssen, S. Harkema, and A. Bantjes, “Elastic modulus in the crystalline region of poly (p-phenylene terephthalamide),” *Polymer*, vol. 17, no. 6, pp. 517–518, 1976.
[33] Y. Termonia and P. Smith, “Theoretical study of the ultimate mechanical properties of poly(p-phenylene-terephthalamide) fibres,” *Polymer*, vol. 27, no. 12, pp. 1845–1849, 1986.
[34] M. Kotera, A. Nakai, M. Saito, T. Izu, and T. Nishino, “Elastic Modulus of the Crystalline Regions of Poly (p-phenylene terephthalamide) Single Fiber Using SPring-8 Synchrotron Radiation,” *Polymer Journal*, vol. 39, no. 12, pp. 1295–1299, 2007.
[35] R. Barton, “Paracrystallinity-Modulus Relationships in Kevlar Aramid Fibers,” *Journal of Macromolecular Science-Physics*, vol. 24, no. 1, pp. 119–130, 1985.
[36] G. C. Rutledge and U. W. Suter, “Detailed Atomistic Simulation of Oriented Pseudocrystalline Polymers and Application to a Stiff-Chain Aramid,” *Macromolecules*, vol. 24, no. 8, pp. 1921–1933, 1991.
[37] G. C. Rutledge and U. W. Suter, “Calculation of mechanical properties of poly(p-phenylene terephthalamide) by atomistic modelling,” *Polymer*, vol. 32, no. 12, pp. 2179–2189, 1991.
[38] U. W. Suter and B. E. Eichinger, “Estimating elastic constants by averaging over simulated structures,” *Polymer*, vol. 43, no. 2, pp. 575–582, Jan. 2002.
[39] K. Nakamae, T. Nishino, and A. Xu, “Poisson's ratio of the crystal lattice of poly(p-phenylene terephthalamide) by X-ray diffraction,” *Polymer*, vol. 33, no. 23, pp. 4898–4900, 1992.
[40] R. J. Young, D. Lu, R. J. Day, W. F. Knoff, and H. A. Davis, “Relationship between structure and mechanical properties for aramid fibers,” *Journal of Materials Science*, vol. 27, no. 20, pp. 5431–5440, 1992.
[41] L. C. Sawyer, R. T. Chen, M. G. Jamieson, I. H. Musselman, and P. E. Russell, “The fibrillar hierarchy in liquid crystalline polymers,” *Journal of Materials Science*, vol. 28, no. 1, pp. 225–238, 1993.
[42] M. Panar, P. Avakian, R. C. Blume, K. H. Gardner, T. D. Gierke, and H. H. Yang, “Morphology of Poly(p-Phenylene Terephthalamide) Fibers,” *Journal of Polymer Science: Polymer Physics Edition*, vol. 21, no. 10, pp. 1955–1969, Oct. 1983.
[43] M. G. Dobb, D. J. Johnson, and B. P. Saville, “Supramolecular Structure of a High-Modulus Polyaromatic Fiber (Kevlar 49),” *Journal of Polymer Science: Polymer Physics Edition*, vol. 15, no. 12, pp. 2201–2211, 1977.
[44] E. J. Roche, S. R. Allen, C. R. Fincher, and C. Paulson, “Macrostructural Deformation of Kevlar 49 Aramid Fibers,” *Molecular Crystals and Liquid Crystals Incorporating Nonlinear Optics*, vol. 153, no. 1, pp. 547–552, 1987.
[45] I. M. Ward, “Optical and Mechanical Anisotropy in Crystalline Polymers,” *Proceedings of the Physical Society of London*, vol. 80, no. 5, pp. 1176–1188, 1962.
[46] M. G. Northolt, “Tensile deformation of poly (p-phenylene terephthalamide)

fibres, an experimental and theoretical analysis," *Polymer*, vol. 21, no. 10, pp. 1199–1204, 1980.
[47] M. G. Northolt and R. van der Hout, "Elastic extension of an oriented crystalline fibre," *Polymer*, vol. 26, no. 2, pp. 310–316, 1985.
[48] J. J. M. Baltussen, M. G. Northolt, and R. van der Hout, "The continuous chain model for the elastic extension of polymer fibers in the glassy state," *Journal of Rheology*, vol. 41, no. 3, pp. 549–573, 1997.
[49] J. J. M. Baltussen and M. G. Northolt, "The elastic extension of polymer fibers in the glassy state: Experimental results," *Journal of Rheology*, vol. 41, no. 3, pp. 575–598, 1997.
[50] S. R. Allen and E. J. Roche, "Deformation behaviour of Kevlar aramid fibres," *Polymer*, vol. 30, no. 6, pp. 996–1003, 1989.
[51] S. R. Allen, "Stress-coupling phenomena in anisotropic fibres," *Polymer*, vol. 29, no. 6, pp. 1091–1094, 1988.
[52] M. G. Northolt, J. J. M. Baltussen, and B. Schaffers-Korff, "Yielding and hysteresis of polymer fibres," *Polymer*, vol. 36, no. 18, pp. 3485–3492, 1995.
[53] J. J. M. Baltussen and M. G. Northolt, "A model for the tensile curve with yield of a polymer fibre," *Polymer Bulletin*, vol. 36, pp. 125–131, 1996.
[54] J. J. M. Baltussen and M. G. Northolt, "The stress and sonic modulus versus strain curve of polymer fibres with yield," *Polymer*, vol. 40, no. 22, pp. 6113–6124, Oct. 1999.
[55] E. P. Socci, D. A. Thomas, R. K. Eby, D. T. Grubb, and W. W. Adams, "Orientation changes in Kevlar 49 under axial compression," *Polymer*, vol. 37, no. 22, pp. 5005–5009, 1996.
[56] S. J. Deteresa, S. R. Allen, R. J. Farris, and R. S. Porter, "Compressive and torsional behaviour of Kevlar 49 fibre," *Journal of Materials Science*, vol. 19, no. 1, pp. 57–72, 1984.
[57] J. W. S. Hearle and B. S. Wong, "Flexural fatigue and surface abrasion of Kevlar-29 and other high-modulus fibres," *Journal of Materials Science*, vol. 12, pp. 2447–2455, 1977.
[58] S. L. Phoenix and J. Skelton, "Transverse Compressive Moduli and Yield Behavior of Some Orthotropic, High-Modulus Filaments," *Textile Research Journal*, vol. 44, no. 12, pp. 934–940, 1974.
[59] J. Singletary, H. Davis, M. K. Ramasubramanian, W. Knoff, and M. Toney, "The transverse compression of PPTA fibers Part I Single fiber transverse compression testing," *Journal of Materials Science*, vol. 35, no. 3, pp. 573–581, 2000.
[60] J. Singletary, H. Davis, Y. Song, M. K. Ramasubramanian, and W. Knoff, "The transverse compression of PPTA fibers Part II Fiber transverse structure," *Journal of Materials Science*, vol. 35, no. 3, pp. 583–592, 2000.
[61] W. F. Knoff, "Relationship between the tensile and shear strength of aramid fibres," *Journal of Materials Science Letters*, vol. 6, no. 12, pp. 1392–1394, 1987.
[62] M. H. Lafitte and A. R. Bunsell, "The creep of Kevlar-29 fibers," *Polymer Engineering & Science*, vol. 25, no. 3, pp. 182–187, Feb. 1985.
[63] A. R. Bunsell, "The tensile and fatigue behaviour of Kevlar-49 (PRD-49)

fibre," *Journal of Materials Science*, vol. 10, no. 8, pp. 1300–1308, 1975.

[64] L. Konopasek and J. W. S. Hearle, "The tensile fatigue behavior of para-oriented aramid fibers and their fracture morphology," *Journal of Applied Polymer Science*, vol. 21, no. 10, pp. 2791–2815, 1977.

[65] H. D. Wagner, P. Schwartz, and S. L. Phoenix, "Lifetime statistics for single Kevlar 49 filaments in creep-rupture," *Journal of Materials Science*, vol. 21, no. 6, pp. 1868–1878, 1986.

[66] H. F. Wu, S. L. Phoenix, and P. Schwartz, "Temperature dependence of lifetime statistics for single Kevlar 49 filaments in creep-rupture," *Journal of Materials Science*, vol. 23, no. 5, pp. 1851–1860, May 1988.

[67] S. R. Allen, E. J. Roche, B. Bennett, and R. Molaison, "Tensile deformation and failure of poly(p-phenylene terephthalamide) fibres," *Polymer*, vol. 33, no. 9, pp. 1849–1854, 1992.

[68] R. H. Ericksen, "Creep of aromatic polyamide fibres," *Polymer*, vol. 26, pp. 733–746, 1985.

[69] R. J. Young, D. Lu, and R. J. Day, "Raman Spectroscopy of Kevlar Fibers During Deformation-Caveat-Emptor," *Polymer International*, vol. 24, no. 2, pp. 71–76, 1991.

[70] M. C. Andrews, R. J. Day, X. Hu, and R. J. Young, "Deformation micromechanics in high-modulus fibres and composites," *Composites Science and Technology*, vol. 48, no. 1, pp. 255–261, 1993.

[71] R. J. Young and M. C. Andrews, "Deformation micromechanics in high-performance polymer fibres and composites," *Materials Science and Engineering A*, vol. 184, no. 2, pp. 197–205, 1994.

[72] R. J. Young, "Monitoring Deformation Processes in High-Performance Fibres using Raman Spectroscopy," *Journal of the Textile Institute*, vol. 86, no. 2, pp. 360–381, 1995.

[73] R. J. Young and S. J. Eichhorn, "Deformation mechanisms in polymer fibres and nanocomposites," *Polymer*, vol. 48, no. 1, pp. 2–18, 2007.

[74] K. Prasad and D. T. Grubb, "Deformation Behavior of Kevlar Fibers Studied by Raman Spectroscopy," *Journal of Applied Polymer Science*, vol. 41, no. 9, pp. 2189–2198, 1990.

[75] C. Zhu, X. Liu, J. Guo, N. Zhao, C. Li, J. Wang, J. Liu, L. Jing, and J. Xu, "Relationship between performance and microvoids of aramid fibers revealed by two-dimensional small-angle X-ray scattering," *Journal of Applied Crystallography*, vol. 46, no. 4, pp. 1178–1186, 2013.

[76] B. R. Pauw, M. E. Vigild, K. Mortensen, J. W. Andreasen, E. A. Klop, D. W. Breiby, and O. Bunk, "Strain-induced internal fibrillation in looped aramid filaments," *Polymer*, vol. 51, no. 20, pp. 4589–4598, Sep. 2010.

[77] K. Vijayan, "Effect of Environmental Exposures on the Aramid Fibre Kevlar," *Metals Materials and Processes*, vol. 12, no. 2, pp. 259–268, 2000.

[78] M. Shubha, H. V. Parimala, and K. Vijayan, "Kevlar 49 fibres: correlation between tensile strength and X-ray diffraction peak positions," *Journal of Materials Science Letters*, vol. 10, no. 23, pp. 1377–1378, 1991.

[79] B. R. Pauw, M. E. Vigild, and K. Mortensen, "Analysing the nanoporous structure of aramid fibres," *Journal of Applied Crystallography*, vol. 43, pp.

837–849, 2010.
[80] H. D. Wagner, S. L. Phoenix, and P. Schwartz, “A Study of Statistical Variability in the Strength of Single Aramid Filaments,” *Journal of Composite Materials*, vol. 18, no. 4, pp. 312–338, 1984.
[81] W. F. Knoff, “A modified weakest-link model for describing strength variability of Kevlar aramid fibres,” *Journal of Materials Science*, vol. 22, pp. 1024–1030, 1987.
[82] W. F. Knoff, “Combined weakest link and random defect model for describing strength variability in fibres,” *Journal of Materials Science*, vol. 28, no. 4, pp. 931–941, 1993.
[83] G. Amaniampong and C. J. Burgoyne, “Statistical variability in the strength and failure strain of aramid and polyester yarns,” *Journal of Materials Science*, vol. 29, no. 19, pp. 5141–5152, 1994.
[84] H. D. Wagner, J. Aronhime, and G. Marom, “Dependence of the tensile strength of pitch-based carbon and para-aramid fibres on the rate of strain,” *Proceedings of the Royal Society London A*, vol. 428, no. 1875, pp. 493–510, 1990.
[85] B. Sanborn, C. A. Gunnarsson, P. Moy, J. Q. Zheng, and T. Weerasooriya, “Effect of Strain Rate and Pre-twist on Strength of Single Kevlar® KM2 Fiber,” presented at the Conference Proceedings of the Society for Experimental Mechanics Series, 2012, pp. 445–447.
[86] G. S. Sheu, T. K. Lin, S. S. Shyu, and J. Y. Lai, “Improvement of adhesion of Kevlar fiber to epoxy by chemical modification,” *Journal of Adhesion Science and Technology*, vol. 8, no. 5, pp. 511–530, 1994.
[87] T. K. Lin, B. H. Kuo, S. S. Shyu, and S. H. Hsiao, “Improvement of the adhesion of Kevlar fiber to bismaleimide resin by surface chemical modification,” *Journal of Adhesion Science and Technology*, vol. 13, no. 5, pp. 545–560, Dec. 1999.
[88] J. H. Kim, N. A. Heckert, S. D. Leigh, H. Kobayashi, W. G. McDonough, K. D. Rice, and G. A. Holmes, “Effects of fiber gripping methods on the single fiber tensile test: I. Non-parametric statistical analysis,” *Journal of Materials Science*, vol. 48, no. 10, pp. 3623–3637, Feb. 2013.
[89] J. H. Kim, N. A. Heckert, S. P. Mates, J. E. Seppala, W. G. McDonough, C. S. Davis, K. D. Rice, and G. A. Holmes, “Effect of fiber gripping method on the single fiber tensile test: II. Comparison of fiber gripping materials and loading rates,” *Journal of Materials Science*, vol. 50, no. 5, pp. 2049–2060, 2015.
[90] K. Şahin, N. A. Fasanella, P. V. Kolluru, and I. Chasiotis, “Mechanical Property Experiments with Ultra-High Strength Micrometer Scale Fibers,” *Experimental Mechanics*, vol. 55, no. 5, pp. 877–885, Feb. 2015.
[91] B. Sanborn, A. M. DiLeonardi, and T. Weerasooriya, “Tensile Properties of Dyneema SK76 Single Fibers at Multiple Loading Rates Using a Direct Gripping Method,” *Journal of Dynamic Behavior of Materials*, vol. 1, pp. 4–14, 2015.
[92] D. J. Sikkema, M. G. Northolt, and B. Pourdeyhimi, “Assessment of new high-performance fibers for advanced applications,” *MRS Bulletin*, pp. 579–

584, 2003.
[93] K. E. Strawhecker and D. P. Cole, “Morphological and local mechanical surface characterization of ballistic fibers via AFM,” *Journal of Applied Polymer Science*, vol. 131, no. 19, 2014.
[94] T. A. Stockdale, K. E. Strawhecker, E. J. Sandoz-Rosado, and E. D. Wetzel, “A rapid FIB-notch technique for characterizing the internal morphology of high-performance fibers,” *Materials Letters*, vol. 176, pp. 173–176, 2016.
[95] J. Lim, J. Q. Zheng, K. Masters, and W. W. Chen, “Effects of gage length, loading rates, and damage on the strength of PPTA fibers,” *International Journal of Impact Engineering*, vol. 38, no. 4, pp. 219–227, 2011.
[96] N. Iosipescu, “New Accurate Procedure for Single Shear Testing of Metals,” *Journal of Materials*, vol. 2, no. 3, pp. 537–566, 1967.
[97] Standard A.S.T.M., “Standard Test Method for Shear Properties of Composite Materials by the V-Notched Beam Method,” ASTM International, West Conshohocken (PA), 2013.
[98] K. Miyauchi, “A proposal of a planar simple shear test in sheet metals,” *Scientific Papers of the Institute of Physical and Chemical Research (Japan)*, vol. 78, no. 3, pp. 27–40, 1984.
[99] Q. Yin, B. Zillmann, S. Suttner, G. Gerstein, M. Biasutti, A. E. Tekkaya, M. F. X. Wagner, M. Merklein, M. Schaper, T. Halle, and A. Brosius, “An experimental and numerical investigation of different shear test configurations for sheet metal characterization,” *International Journal of Solids and Structures*, vol. 51, no. 5, pp. 1066–1074, 2014.
[100] Q. Yin, C. Soyarslan, K. Isik, and A. E. Tekkaya, “A grooved in-plane torsion test for the investigation of shear fracture in sheet materials,” *International Journal of Solids and Structures*, vol. 66, pp. 121–132, Jan. 2015.
[101] Standard A.S.T.M., “Standard Test Method for Shear Testing of Aluminum Alloy Products,” ASTM International, West Conshohocken, PA, 2014.
[102] D. Rittel, S. Lee, and G. Ravichandran, “A Shear-Compression Specimen for Large Strain Testing,” *Experimental Mechanics*, vol. 42, no. 1, pp. 58–64, 2002.
[103] D. Rittel, G. Ravichandran, and S. Lee, “Large strain constitutive behavior of OFHC copper over a wide range of strain rates using the shear compression specimen,” *Mechanics of Materials*, vol. 34, no. 10, pp. 627–642, 2002.
[104] G. Gruben, E. Fagerholt, O. S. Hopperstad, and T. Børvik, “Fracture characteristics of a cold-rolled dual-phase steel,” *European Journal of Mechanics, A/Solids*, vol. 30, no. 3, pp. 204–218, 2011.
[105] A. Abedini, C. Butcher, and M. J. Worswick, “Fracture Characterization of Rolled Sheet Alloys in Shear Loading: Studies of Specimen Geometry, Anisotropy, and Rate Sensitivity,” *Experimental Mechanics*, vol. 57, no. 1, pp. 75–88, 2017.
[106] V. Tarigopula, O. S. Hopperstad, M. Langseth, A. H. Clausen, F. Hild, O. G. Lademo, and M. Eriksson, “A Study of Large Plastic Deformations in Dual Phase Steel Using Digital Image Correlation and FE Analysis,” *Experimental Mechanics*, vol. 48, no. 2, pp. 181–196, 2008.

[107] M. Brünig, O. Chyra, D. Albrecht, L. Driemeier, and M. Alves, "A ductile damage criterion at various stress triaxialities," *International Journal of Plasticity*, vol. 24, no. 10, pp. 1731–1755, 2008.

[108] O. G. Lademo, O. Engler, S. Keller, T. Berstad, K. O. Pedersen, and O. S. Hopperstad, "Identification and validation of constitutive model and fracture criterion for AlMgSi alloy with application to sheet forming," *Materials and Design*, vol. 30, no. 8, pp. 3005–3019, 2009.

[109] A. Reyes, M. Eriksson, O. G. Lademo, O. S. Hopperstad, and M. Langseth, "Assessment of yield and fracture criteria using shear and bending tests," *Materials and Design*, vol. 30, no. 3, pp. 596–608, 2009.

[110] J. Peirs, P. Verleysen, and J. Degrieck, "Novel Technique for Static and Dynamic Shear Testing of Ti6Al4V Sheet," *Experimental Mechanics*, vol. 52, no. 7, pp. 729–741, 2012.

[111] F. Gao, L. Gui, and Z. Fan, "Experimental and Numerical Analysis of an In-Plane Shear Specimen Designed for Ductile Fracture Studies," *Experimental Mechanics*, vol. 51, no. 6, pp. 891–901, 2011.

[112] M. Isakov, J. Seidt, K. Östman, A. Gilat, and V. T. Kuokkala, "Characterization of a Ferritic Stainless Sheet Steel in Simple Shear and Uniaxial Tension at Different Strain Rates," presented at the ASME 2011 International Mechanical Engineering Congress and Exposition, IMECE 2011, 2011, vol. 8, pp. 101–109.

[113] Y. Bao and T. Wierzbicki, "On fracture locus in the equivalent strain and stress triaxiality space," *International Journal of Mechanical Sciences*, vol. 46, no. 1, pp. 81–98, 2004.

[114] J. Lian, M. Sharaf, F. Archie, and S. Münstermann, "A hybrid approach for modelling of plasticity and failure behaviour of advanced high-strength steel sheets," *International Journal of Damage Mechanics*, vol. 22, no. 2, pp. 188–218, 2013.

[115] J. Kang, D. S. Wilkinson, P. D. Wu, M. Bruhis, M. Jain, J. D. Embury, and R. K. Mishra, "Constitutive Behavior of AA5754 Sheet Materials at Large Strains," *Journal of Engineering Materials and Technology, Transactions of the ASME*, vol. 130, no. 3, pp. 0310041–0310045, 2008.

[116] K. A. Gardner, J. D. Seidt, M. Isakov, and A. Gilat, "Characterization of sheet metals in shear over a wide range of strain rates," presented at the Conference Proceedings of the Society for Experimental Mechanics Series, 2014, vol. 1, pp. 313–317.

[117] L. C. S. Nunes, "Modified slotted shear test for a thin sheet of solid polymer under large deformations," *Polymer Testing*, vol. 45, pp. 20–30, May 2015.

[118] L. Denk, H. Hatta, A. Misawa, and S. Somiya, "Shear fracture of C/C composites with variable stacking sequence," *Carbon*, vol. 39, no. 10, pp. 1505–1513, 2001.

[119] K. A. Slusarksi, M. S. Walter, T. A. Bogetti, and E. D. Wetzel, "In-plane shear properties of high-performance filaments," presented at the Conference Proceedings of the Society for Experimental Mechanics Series, 2014, vol. 7, pp. 91–96.

[120] M. Cheng, W. Chen, and T. Weerasooriya, "Mechanical Properties of Kevlar

KM2 Single Fiber," *Journal of Engineering Materials and Technology*, vol. 127, pp. 197–203, 2005.

[121] S. R. Allen, "Tensile recoil measurement of compressive strength for polymeric high performance fibres," *Journal of Materials Science*, vol. 22, no. 3, pp. 853–859, 1987.

[122] I. Utke, S. Moshkalev, and P. Russell, *Nanofabrication Using Focused Ion and Electron Beams*. Oxford University Press, 2012.

[123] M. Naraghi, I. Chasiotis, H. Kahn, Y. Wen, and Y. Dzenis, "Novel method for mechanical characterization of polymeric nanofibers," *Review of Scientific Instruments*, vol. 78, no. 85108, p. 085108, 2007.

[124] M. Naraghi, I. Chasiotis, H. Kahn, Y. Wen, and Y. Dzenis, "Mechanical deformation and failure of electrospun polyacrylonitrile nanofibers as a function of strain rate," *Applied Physics Letters*, vol. 91, no. 15901, 2007.

[125] J. T. Dickinson, L. C. Jensen, and M. L. Klakken, "Electron-beam-induced fracture of Kevlar single fibers," *Journal of Vacuum Science and Technology A: Vacuum, Surfaces and Films*, vol. 4, no. 3, pp. 1501–1504, 1986.